



UNIVERSITY OF LEEDS

This is a repository copy of *Changes in elevation and mass of Arctic glaciers and ice caps, 2010–2017*.

White Rose Research Online URL for this paper:
<https://eprints.whiterose.ac.uk/176412/>

Version: Accepted Version

Article:

Tepes, P, Gourmelen, N, Nienow, P et al. (3 more authors) (2021) Changes in elevation and mass of Arctic glaciers and ice caps, 2010–2017. *Remote Sensing of Environment*, 261. 112481. ISSN 0034-4257

<https://doi.org/10.1016/j.rse.2021.112481>

© 2021, Elsevier. This manuscript version is made available under the CC-BY-NC-ND 4.0 license <http://creativecommons.org/licenses/by-nc-nd/4.0/>.

Reuse

This article is distributed under the terms of the Creative Commons Attribution-NonCommercial-NoDerivs (CC BY-NC-ND) licence. This licence only allows you to download this work and share it with others as long as you credit the authors, but you can't change the article in any way or use it commercially. More information and the full terms of the licence here: <https://creativecommons.org/licenses/>

Takedown

If you consider content in White Rose Research Online to be in breach of UK law, please notify us by emailing eprints@whiterose.ac.uk including the URL of the record and the reason for the withdrawal request.



eprints@whiterose.ac.uk
<https://eprints.whiterose.ac.uk/>

1 **Changes in elevation and mass of Arctic glaciers and ice caps, 2010-2017**

2 **P. Tepes¹, N. Gourmelen^{1,2}, P. Nienow¹, M. Tsamados³, A. Shepherd⁴, and F. Weissgerber¹**

3 School of GeoSciences, University of Edinburgh, UK.

4 ²IPGS UMR 7516, Université de Strasbourg, CNRS, Strasbourg, France.

5 ³Centre for Polar Observation and Modeling, University College London, London, UK.

6 ⁴Centre for Polar Observation and Modelling, School of Earth and Environment, University of
7 Leeds, Leeds, UK.

8 Corresponding author: Paul Tepes (paul.tepes@ed.ac.uk)

9 **Key words:**

- 10 • Arctic glaciers and ice caps
11 • Mass balance
12 • Arctic warming
13 • CryoSat-2
14 • Swath processing

1 **Abstract**

2 Arctic glaciers and ice caps (GIC) are losing mass rapidly, and this process is expected to
3 continue during the 21st century owing to polar amplification of climate warming. Here, we use
4 seven years of CryoSat-2 swath interferometric altimetry to track changes in the volume of Arctic
5 GIC. From these data, we produce a pan-Arctic assessment of GIC mass imbalance, and we
6 partition their losses into signals associated with atmospheric processes and glacier dynamics.
7 Between 2010 and 2017, Arctic GIC lost 609 ± 7 Gt of ice, contributing 0.240 ± 0.007 millimetres
8 per year to global sea level rise. While surface ablation is responsible for 87% of losses across
9 the Arctic, dynamic imbalance is increasing in the Barents and Kara Sea region where it now
10 accounts for 43% of total ice loss. Arctic GIC's dynamic imbalance is associated with a northward
11 shift of Atlantic climate, and this effect should be considered in global sea level projections.

12

13 **1. Introduction**

14 Arctic glaciers and ice caps (GIC) are key players in the local freshwater budget, impact
15 thermohaline forcing in the North Atlantic (Thornalley et al., 2018; Yang et al., 2016), and are
16 significant contributors to global eustatic sea level rise (Ciraci et al., 2020; Gardner et al., 2013;
17 Zemp et al., 2019). They store 40% of the global GIC ice volume, equating to 144 mm of sea level
18 equivalent (Farinotti et al., 2019), and their losses are currently increasing as atmospheric and
19 oceanic forcing intensify (Barton et al., 2018; Ding et al., 2014) and as Arctic sea ice cover shrinks
20 (Onarheim et al., 2018). Furthermore, the dynamic response of land ice to climate forcing
21 constitutes the main uncertainty in global sea level projections for the next century (Church, 2013;
22 Martin and Adcroft, 2010). To address this knowledge gap, observations of the relative
23 contribution of both surface mass balance (SMB) and ice dynamics (D) to the total losses are
24 necessary. A recent study finds that between 1972 and 2018, D accounted for 66% of the total

1 mass imbalance of the Greenland Ice Sheet (Mouginot et al., 2019). For the GIC of the Arctic
2 however, the SMB-to-D ratio is unknown.

3 SMB is determined by thermodynamic processes at the ice surface, and is modified by
4 shifts in large-scale atmospheric circulation patterns (Delhasse et al., 2018) and by CO₂-induced
5 radiative forcing (Byrne and Schneider, 2018; Shindell and Faluvegi, 2009). In addition to negative
6 overall SMB, the Arctic GIC mass imbalance was amplified in recent years by the large-scale
7 destabilisation of marine-terminating drainage basins, during which ice flux to the ocean was
8 locally increased by several orders of magnitude (Haga et al., 2020; McMillan et al., 2014; Nuth
9 et al., 2019; Strozzi et al., 2017a; Willis et al., 2018). The persistent incursion of warm North
10 Atlantic Ocean water into the Arctic Ocean is thought to have direct impact on sea ice extent and
11 tidewater glacier dynamics (Barton et al., 2018; McMillan et al., 2014; Polyakov et al., 2017). The
12 respective role of internal processes, commonly ascribed to glacier surges, and external climatic
13 forcing in driving these dynamic instabilities remains largely unclear (Dunse et al., 2015; McMillan
14 et al., 2014). The relative impact of atmospheric and oceanic influences on glacier fluctuations at
15 the ice-ocean interface is also uncertain, with potential control from both oceanic heat transport
16 and surface runoff (Cowton et al., 2018). Here, we use CryoSat-2 swath interferometric altimetry
17 (Foresta et al., 2016; Gourmelen et al., 2018) to measure changes in the volume of Arctic GIC
18 with unprecedented spatial resolution and to partition the observed changes into signals
19 associated with atmospheric processes, via SMB, and glacier dynamics.

20

21 **2. Pan-arctic view of GIC thinning**

22 We derive rates of change in land ice surface elevation \dot{h} in all areas of the Arctic beyond
23 Greenland. This includes the southern and northern Canadian Arctic Archipelagos (CAA-S and
24 CAA-N, respectively), Iceland (Ic), Svalbard (Sv), and the Russian Arctic Archipelagos (RAA) of
25 Franz Josef Land (FJL), Novaya Zemlya (NZ) and Severnaya Zemlya (SZ) (Fig. 1). We apply

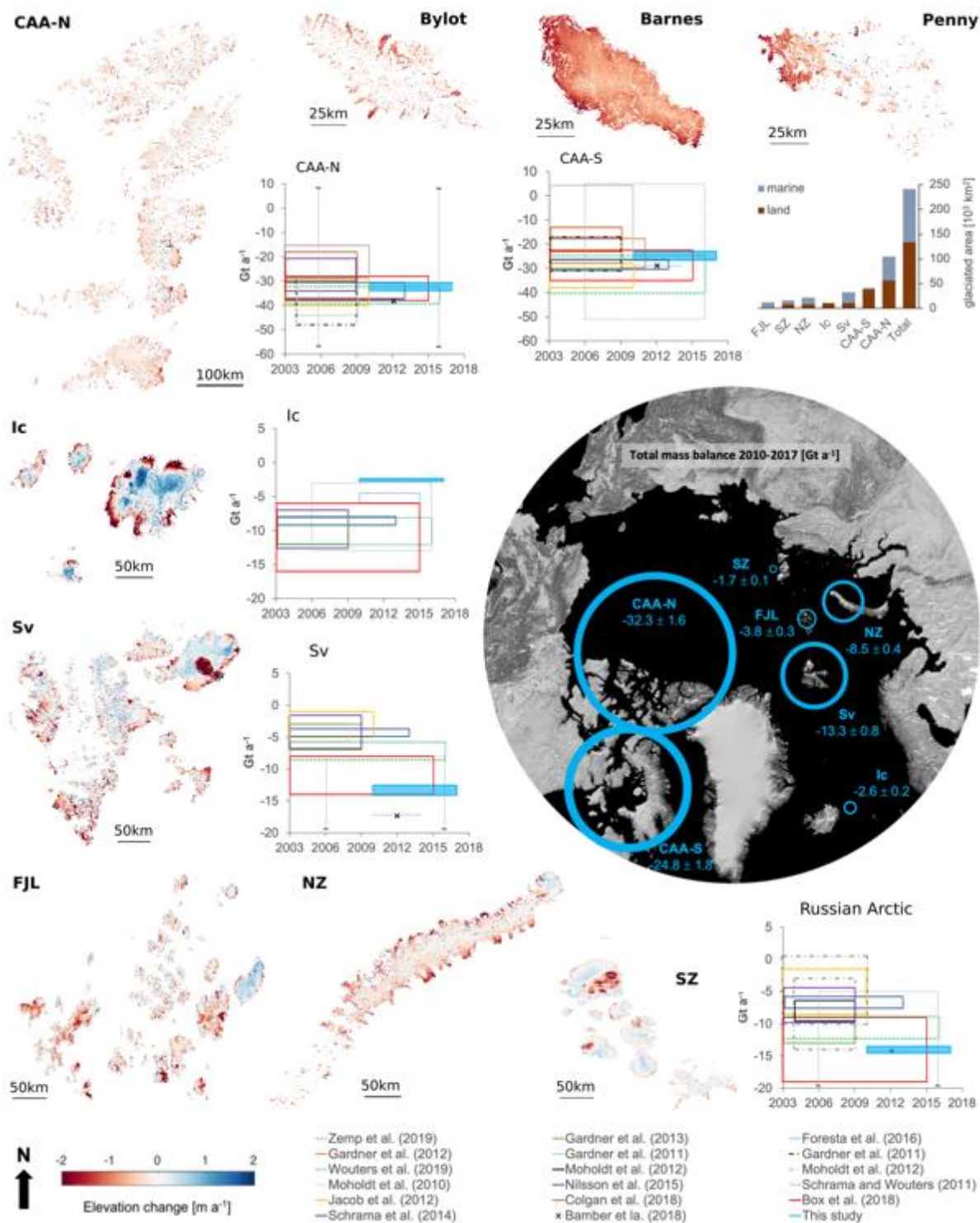


Fig. 1. Rates of \dot{h} (expanded maps available in Appendices C1-C6), glaciated area of marine- and land-terminating glacier catchments, and Arctic GIC mass balance represented in graphical form as boxes indicating average values over their respective study period (width) with error estimates (height). A map of the Arctic shows the location of GIC and mass balance from the present study represented by circles with size proportional to the mass losses and their width proportional to the error budget.

1 swath processing to CryoSat-2 altimetry data spanning the period 2010-2017 to retrieve time-
2 dependent elevation measurements over the GIC (Gourmelen et al., 2018). The high density of
3 observations enables us to compute mean \dot{h} over unit areas of 500 by 500 m to ensure sufficient
4 spatial detail while maximising the number of observations in each resolution cell (Foresta et al.,
5 2016) (Appendix A1-A3). Regionally, this translates into a ratio of measured-to-total glaciated
6 area equal to 83% over the GIC of the Russian Arctic, 79% over Svalbard and Iceland, and 60%
7 over the Canadian Arctic, with good coverage over the ice margins (Appendices B and C).

8 Ice thinning is widespread across the Arctic, and the median rate of elevation change is -
9 0.25 m a^{-1} . There is, however, considerable spatial variability, and the 5% and 95% quantiles are
10 -1.65 m a^{-1} and $+0.70 \text{ m a}^{-1}$ respectively, reflecting the diversity of responses of ice masses to
11 forcing across the Arctic (Fig. 1).

12 The climate of the southern and northern Canadian Arctic Archipelagos exhibits low inter-
13 annual variability in precipitation but high variability in summer surface temperatures (Gardner et
14 al., 2012), which results in spatially homogeneous thinning patterns, driven largely by changes in
15 summer surface melt rates (Gardner et al., 2012, 2011). Median thinning rates over CAA-S (0.75
16 m a^{-1}) are three times larger than over CAA-N (0.24 m a^{-1}), reflecting the latitudinal control on
17 SMB. Rates of thinning of up to 5 m a^{-1} are observed at low elevations and over a limited number
18 of marine-terminating outlet glaciers, including on Devon Ice Cap and Prince of Wales Icefield
19 (Appendices C6c and C6e, respectively). The strongest spatially extensive thinning signal across
20 CAA-S is from the ablation zone of Barnes and Penny Ice Caps where thinning rates are in excess
21 of 2.5 m a^{-1} (Fig. 1). Icelandic ice caps display diverse patterns of glacier change (Fig. 1), reflecting
22 in part their location over volcanically active terrain, frequent surges, and high variability in climate
23 patterns (Foresta et al., 2016). Nevertheless, between 2010 and 2017, they have mainly
24 experienced SMB-driven ice loss, with strong seasonal trends and high melt rates of up to 6 m a^{-1}
25 1 along ice cap margins and thickening in the accumulation zones driven by post-surge dynamic

1 responses and exceptionally large winter accumulation in recent years (Foresta et al., 2016;
2 Wouters et al., 2019).

3 Complex patterns of change also prevail over the archipelagos of the Barents and Kara
4 Sea (BKS) region, including Svalbard and the Russian Arctic Archipelagos, where rates of \dot{h} have
5 high spatial variability (Fig. 1). Pronounced thinning ($> 1 \text{ m a}^{-1}$) is observed at a large number of
6 marine-terminating glacier catchments, which overall represent 66% of the total glaciated area in
7 the BKS. Examples of increased thinning associated with dynamic change include an increasing
8 number of marine-terminating basins in Svalbard, such as along the southeastern flanks of
9 Austfonna Ice Cap, including Basin 3 (McMillan et al., 2014), and the frontal destabilisation of
10 Stonebreen, Edgeøya (Strozzi et al., 2017a). In Severnaya Zemlya, six basins are thinning at an
11 average rate (0.85 m a^{-1}) an order of magnitude higher than the rest of the archipelago (0.08 m
12 a^{-1}), all six of which are marine-terminating catchments located primarily around the southern and
13 eastern flanks of the Academy of Sciences Ice Cap (Moholdt et al., 2012a; Sánchez-Gómez et
14 al., 2019), and one on the western flank of Vavilov Ice Cap (Willis et al., 2018) (Appendix C4).
15 Fed by ice streams from the Karpinsky and Rusanov Ice Caps (Appendix C4), the collapse of the
16 Matusевич Ice Shelf in 2012 triggered the rapid acceleration of two main outlet glaciers of
17 Karpinsky Ice Cap, one having sped up by up to 200% at its terminus between 2010 and 2014
18 (Willis et al., 2015). Windy Ice Cap on Graham Bell Island, the easternmost ice cap in Franz Josef
19 Land (Appendix C2), represents a singularity in the archipelago, thickening at an average rate of
20 0.4 m a^{-1} , thereby maintaining a positive trend since the 1950s (Moholdt et al., 2012b; Zheng et
21 al., 2018).

22

23 **3. Arctic GIC mass balance**

24 We convert elevation to volume change using glacier area extents from the Randolph Glacier
25 Inventory (RGI 6.0) and we derive mass budgets (Appendices A5-A7) using an assumed constant

1 density of ice ρ_{ice} equal to $850 \pm 60 \text{ kg m}^{-3}$ (Huss, 2013) (Table 1). Between 2010 and 2017, Arctic
 2 GIC outside of Greenland lost on average $87.0 \pm 2.6 \text{ Gt}$ of ice per year (Fig. 1, Table 1),
 3 corresponding to a mean sea level contribution of $+0.240 \pm 0.007 \text{ mm a}^{-1}$. The largest losses
 4 occurred over the Canadian Arctic, with mass trends of $-32.3 \pm 1.6 \text{ Gt a}^{-1}$ and $-24.8 \pm 1.8 \text{ Gt a}^{-1}$
 5 for CAA-N and CAA-S, respectively. The largest loss per unit area is for CAA-S ($606 \pm 44 \text{ kg m}^{-2}$
 6 a^{-1}), followed by Svalbard ($401 \pm 24 \text{ kg m}^{-2} \text{ a}^{-1}$), Novaya Zemlya ($385 \pm 18 \text{ kg m}^{-2} \text{ a}^{-1}$), CAA-N (308
 7 $\pm 15 \text{ kg m}^{-2} \text{ a}^{-1}$), Franz Josef Land ($297 \pm 23 \text{ kg m}^{-2} \text{ a}^{-1}$), and Iceland ($234 \pm 18 \text{ kg m}^{-2} \text{ a}^{-1}$). Specific
 8 mass loss over Severnaya Zemlya ($-106 \pm 6 \text{ kg m}^{-2} \text{ a}^{-1}$) is the lowest in the Arctic, representing
 9 $\sim 1/4$ of the rate of loss over Novaya Zemlya and $\sim 1/3$ that of Franz Josef Land.

Table 1

Summary table of mass budget: total mass balance and cumulative contributions to sea level rise (SLR) of Arctic GIC from 2010 to 2017.

Region	Total area* [10^3 km^2]	Mass budget** [Gt a^{-1}] 2003-2009	Mass budget*** [Gt a^{-1}] 2010-2017	Mass budget [$\text{kg m}^{-2} \text{ a}^{-1}$] 2010-2017	SLR [mm a^{-1}] 2010-2017
FJL	12.8	-0.6 ± 0.9	$-3.8 (-4.0) \pm 0.3$	-297 ± 23	$+0.010 \pm 0.001$
NZ	22.1	-7.1 ± 1.2	$-8.5 (-9.0) \pm 0.4$	-385 ± 18	$+0.024 \pm 0.001$
SZ	16.0	-1.4 ± 0.9	$-1.7 (-1.8) \pm 0.1$	-106 ± 6	$+0.005 \pm 0.000$
Sv	33.2	-5 ± 2	$-13.3 (-14.1) \pm 0.8$	-401 ± 24	$+0.037 \pm 0.002$
Ic	11.1	-10 ± 2	$-2.6 (-2.8) \pm 0.2$	-234 ± 18	$+0.007 \pm 0.001$
CAA-N	105.0	-33 ± 4	$-32.3 (-34.2) \pm 1.6$	-308 ± 15	$+0.089 \pm 0.004$
CAA-S	40.9	-27 ± 4	$-24.8 (-26.3) \pm 1.8$	-606 ± 44	$+0.068 \pm 0.005$
RAA	50.9	-11 ± 4	$-14.0 (-14.8) \pm 0.5$	-275 ± 10	$+0.039 \pm 0.001$
BKS	84.1	-16 ± 4	$-27.3 (-28.9) \pm 0.9$	-325 ± 11	$+0.075 \pm 0.002$
CAA	145.9	-60 ± 6	$-57.1 (-60.5) \pm 2.4$	-391 ± 16	$+0.186 \pm 0.008$
Total Arctic	241.1	-86 ± 7	$-87.0 (-92.1) \pm 2.6$	-361 ± 11	$+0.240 \pm 0.007$

* Total glaciated area (RGI 6.0), ** mass budgets using a constant density of ice equal to 900 kg m^{-3} (Gardner et al., 2013) for RAA, Sv, Ic, CAA-N and CAA-S, and (Moholdt et al., 2012b) for NZ, SZ and FJL, which cover the period 2004–2009), *** mass budgets using a constant density of ice at 850 kg m^{-3} (900 kg m^{-3} for comparison with the 2003-2009 mass budget estimates).

10 Our measurements reveal an increase in mean annual ice loss of 7% between the 2003-
 11 2009 ICESat period (Gardner et al., 2013) and our 2010-2017 study period. However, this overall
 12 mass loss hides contrasting patterns of change across the regions. While during 2010-2017, the

1 Canadian Arctic has seen a rate of loss comparable to the period between 2003 and 2009, Iceland
2 glaciers have lost mass at a lower rate, due primarily to recent record rates of winter accumulation
3 leading locally to positive SMB (Foresta et al., 2016; Wouters et al., 2019). The largest increase
4 in rates of mass loss occurred within the BKS sector. Rates of ice loss over Svalbard, for example,
5 almost trebled over the CryoSat-2 measurement period ($13.3 \pm 0.8 \text{ Gt a}^{-1}$) compared to the
6 previous six years (Gardner et al., 2013). In the Russian Arctic, Franz Josef Land went from near-
7 balance conditions during the 2004-2009 period ($0.6 \pm 0.9 \text{ Gt a}^{-1}$, Table 1) to considerable mass
8 loss during 2010-2017 ($3.8 \pm 0.3 \text{ Gt a}^{-1}$), and up to $4.4 \pm 0.8 \text{ Gt a}^{-1}$ during 2011-2016 (Zheng et
9 al., 2018). Novaya Zemlya remained the largest contributor to sea level change in the Russian
10 Arctic, losing $8.5 \pm 0.4 \text{ Gt a}^{-1}$ between 2010 and 2017. This is 27% more ice loss per year
11 compared to 2004-2009 (Moholdt et al., 2012b), and 80% more than the 60-year average ($5.1 \pm$
12 0.8 Gt a^{-1}) (Melkonian et al., 2016). Our mass balance estimate for Novaya Zemlya coincides with
13 the 2012-2013/14 rate (-8.5 Gt a^{-1}) from WorldView stereo-pair imagery (Melkonian et al., 2016),
14 and is similar to a longer-term (2002-2016) mean of $-8 \pm 4 \text{ Gt a}^{-1}$ derived from a combination of
15 IceSat, GRACE and CryoSat-2 measurements (Ciraci et al., 2018). It is however lower, although
16 within error margins, compared with Ciraci et al.'s 2010-2016 estimate ($-13.3 \pm 5 \text{ Gt a}^{-1}$) using
17 conventional CryoSat-2 point-of-closest-approach processing (Ciraci et al., 2018). Severnaya
18 Zemlya's rate of loss was similar (29% increase) to the previous decade, reaching $1.7 \pm 0.1 \text{ Gt a}^{-1}$
19 in 2010-2017 (Table 1). Overall, GIC within the BKS sector have released an extra 100 km^3 of
20 freshwater to the ocean between 2010 and 2017 compared to the previous decade, a volume
21 similar in magnitude to that associated with receding sea ice cover in this region (Labe et al.,
22 2018; Onarheim et al., 2018).

23

1 4. Surface mass balance and glacier dynamics

2 Over land-terminating GIC, elevation change rates \dot{h} can be related directly to the local SMB
3 anomaly (Fig. 2a). It is thereby assumed that surface processes dominate the mass loss, and
4 dynamic thickness changes resulting from glacier surges are either negligible, or leveling out
5 across the entire area A_l of land-terminating basins, such that $\dot{h}_l \approx SMB_l / (A_l * \rho_{ice})$. To quantify
6 the relative contribution of SMB and D to the overall mass loss for each of the seven regions listed
7 in Table 1, we first parametrise elevation change \dot{h}_l over land-terminating GIC as a function of
8 first-order controls on SMB_l , that is elevation (h_l), and spatial coordinates (x_l, y_l) :

$$9 \quad \dot{h}_l \approx a_0 h_l^3 + a_1 h_l^2 + a_2 h_l + a_3 x_l + a_4 y_l + a_5$$

10 We then use our parametrisation to *i*) estimate bulk SMB_m over marine-terminating sectors, and
11 *ii*) derive a bulk loss of D by subtracting SMB_m from the total marine-terminating GIC mass balance
12 (Appendix A8). A comparison between our derived SMB and that of the regional atmospheric
13 climate model RACMO2.3 over land-terminating GIC in the Canadian Arctic (Noël et al., 2018)
14 demonstrates an excellent agreement (Fig. 2b, Appendix A9). It also highlights the ability of our
15 parametrisation to capture the first order SMB dependency on elevation and geographical location
16 resulting in SMB variability between land- and adjacent marine-terminating sectors (Fig. 2a,c).
17 Figure 2c illustrates the spatial distribution of the partitioning after extracting the SMB_m signal over
18 marine-terminating basins in two key regions of the Arctic where dynamic thinning has been a
19 key mechanism of ice loss during the 2010s, namely Austfonna Ice Cap (Dunse et al., 2015) and
20 Severnaya Zemlya (Sánchez-Gómez et al., 2019; Zheng et al., 2019).

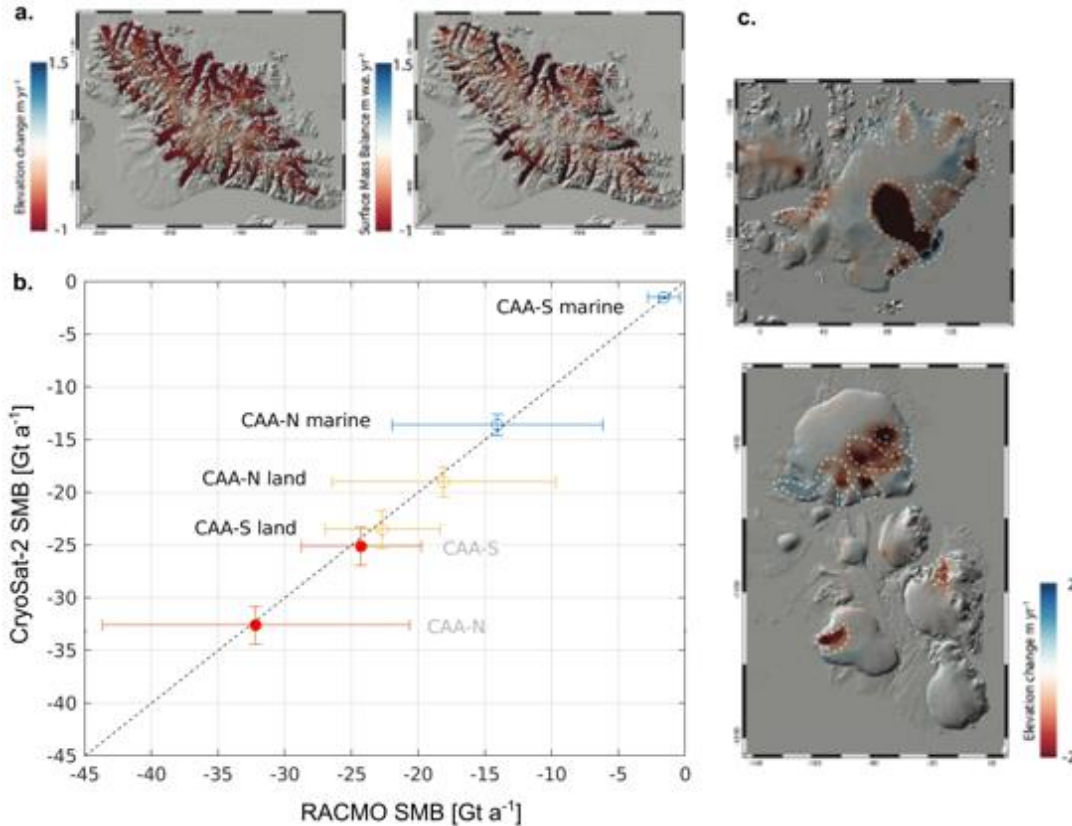


Fig. 2. **a.** CryoSat-2 derived \dot{h} (left) versus RACMO2.3 SMB (right) over Bylot Island, CAA-S; **b.** SMB from CryoSat-2 versus RACMO2.3 across the Canadian Arctic: all regions (red), land-terminating sectors (yellow), marine-terminating sectors (blue); **c.** dynamic thinning $\dot{h} - \dot{h}_{pm}$ (Appendix A8) over major BKS flow units: Austfonna Ice Cap (upper panel) and Severnaya Zemlya archipelago (lower panel). The white dashed lines indicate areas of dynamic thinning.

1 We observe an increasingly negative area-specific SMB with distance from the pole over
 2 the Canadian Arctic (Fig. 3). In contrast, a simple latitudinal control on SMB is not apparent across
 3 the archipelagos east of Greenland, reflecting the more complex interplay between atmospheric
 4 and oceanic influences. Noteworthy are the Sv-FJL-SZ and NZ-SZ gradients of SMB, with less
 5 negative values in north-eastward direction resulting from decreasing incursions of hot, moist
 6 Atlantic air masses (Moholdt et al., 2012b). Finally, our results confirm that SMB dominates the
 7 total mass budget west of Greenland, with insignificant contribution from D ($D \sim 0$). According to
 8 Millan et al. (2017) this contribution has been decreasing since the early 1990s.

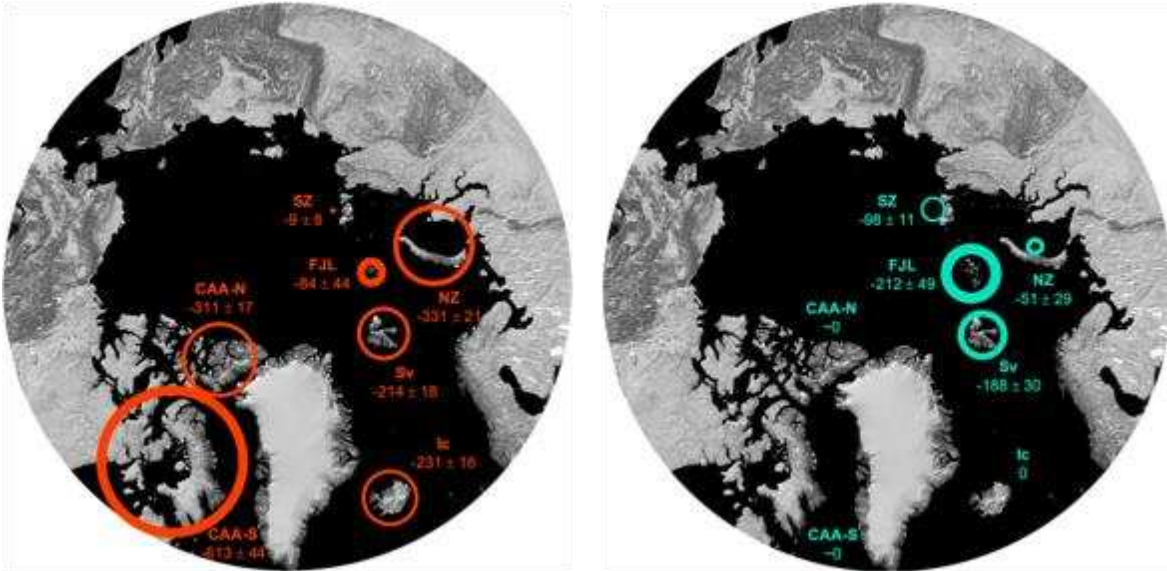


Fig. 3. Area-specific mass balance in [kg m⁻² a⁻¹]: SMB (orange, left) and D (cyan, right), derived from CryoSat-2. Circles with size proportional to ice mass losses and their width proportional to the corresponding error budget.

1

2 The regional differences in the dynamic component *D* contrast significantly with SMB, with

3 a pronounced and strong imbalance in the BKS region compared with the rest of the Arctic (Fig.

4 3). Between 2010 and 2017, ice losses in the BKS sector were nearly two times larger per unit

5 area from marine-terminating ($384 \pm 16 \text{ kg m}^{-2} \text{ a}^{-1}$) than from land-terminating basins (209 ± 10

6 $\text{kg m}^{-2} \text{ a}^{-1}$). Although an Arctic-wide partitioning between SMB and *D* is not available before 2010,

7 the disparity between losses from land- and marine-terminating GIC must have increased

8 compared to the 2000s, considering the acceleration of tidewater glaciers in recent years (Nuth

9 et al., 2019; Strozzi et al., 2017b) and the rapid deflation of a small number of marine-terminating

10 basins (Dunse et al., 2015; Haga et al., 2020; McMillan et al., 2014; Nuth et al., 2019; Strozzi et

11 al., 2017a; Willis et al., 2018). Austfonna Ice Cap alone lost $4.6 \pm 0.3 \text{ Gt a}^{-1}$ during 2010-2017, a

12 budget dominated by the dynamic activation of Basin 3 since 2012 (McMillan et al., 2014)

13 (Appendix B). In Severnaya Zemlya, where SMB represents only 6% of total mass loss, ice

14 dynamics were largely responsible for the negative regional losses between 2010 and 2017

15 (Table 2), with dynamic thinning dominating mass balance fluctuations in this region since the

1 1990s (Moholdt et al., 2012a). Elsewhere in the BKS sector, ice discharge accounted for 72%,
 2 47% and 13% of the total mass loss for Franz Josef Land, Svalbard and Novaya Zemlya
 3 respectively (Table 2). By unit area, Franz Josef Land, Svalbard and Severnaya Zemlya exhibit
 4 the largest rates of dynamic loss D with $212 \pm 49 \text{ kg m}^{-2} \text{ a}^{-1}$, $188 \pm 30 \text{ kg m}^{-2} \text{ a}^{-1}$ and $98 \pm 11 \text{ kg m}^{-2} \text{ a}^{-1}$, respectively (Table 2, Fig. 3). Some of Novaya Zemlya's Barents Sea coast outlet glaciers
 5 accelerated during the study period (Carr et al., 2017; Melkonian et al., 2016), contributing to a
 6 dynamic imbalance of $-51 \pm 29 \text{ kg m}^{-2} \text{ a}^{-1}$. By unit marine-terminating basin area, which highlights
 7 the intensity of dynamic instability, Svalbard lost ice via discharge at $277 \pm 41 \text{ kg m}^{-2} \text{ a}^{-1}$ owing
 8 mainly to Basin 3, followed by Franz Josef Land at $235 \pm 54 \text{ kg m}^{-2} \text{ a}^{-1}$, Severnaya Zemlya at 205
 9 $\pm 20 \text{ kg m}^{-2} \text{ a}^{-1}$ and Novaya Zemlya at $82 \pm 37 \text{ kg m}^{-2} \text{ a}^{-1}$ (Table 2).

Table 2

Summary table of D : the dynamic mass budget is calculated with a constant density of ice equal to 850 kg m^{-3} . Area-specific D is computed relative to the total marine-terminating basin area (*) and relative to the total glaciated area (**) of each region. The last column refers to D as a percentage of total mass balance (\dot{m}).

Region	D [Gt a ⁻¹]	D_{spec} [kg m ⁻² a ⁻¹]*	D_{spec} [kg m ⁻² a ⁻¹ **	D / \dot{m}
FJL	-2.7 ± 0.6	-235 ± 54	-212 ± 49	72 %
NZ	-1.1 ± 0.5	-82 ± 37	-51 ± 29	13 %
SZ	-1.6 ± 0.2	-205 ± 20	-98 ± 11	94 %
Sv	-6.2 ± 0.9	-277 ± 41	-188 ± 30	47 %
lc	-	-	-	-
CAA-N	$+0.3 \pm 1.4$	$+7 \pm 28$	$+3 \pm 23$	1 %
CAA-S	$+0.3 \pm 0.4$	$+93 \pm 137$	$+7 \pm 63$	1 %
RAA	-5.4 ± 0.8	-164 ± 25	-108 ± 18	38 %
BKS	-11.6 ± 1.2	-210 ± 22	-138 ± 16	43 %
Total Arctic	-11.0 ± 1.9	-102 ± 17	-46 ± 16	13

11

5. Atmospheric and oceanic drivers of ice loss

Although atmospheric warming is the primary cause of ice loss from the surface of Arctic GIC through increased melting (e.g. Gardner et al., 2011), a broad range of factors affect their discharge. Tidewater glacier dynamics are determined by changing boundary conditions such as shifts in the stress balance at the glacier front, as these can trigger instabilities that can propagate inland rapidly (Dunse et al., 2015; McMillan et al., 2014; Nuth et al., 2019; Willis et al., 2018). The influx of Atlantic Ocean waters and recirculation of warm bottom water in Arctic fjords, the rapid drainage of surface meltwater to the base of glaciers, and submarine melting driven by the buoyant advection of subglacial discharge at calving fronts, are all known to affect rates of tidewater glacier flow (Cook et al., 2019; Cowton et al., 2018; Slater et al., 2016). Decreased sea ice concentrations have also been suggested to impact calving rates and promote the acceleration of ice discharge (Robel, 2017). To investigate the drivers of the recent Arctic GIC dynamic imbalance, we analyse trends in regional atmospheric (Dee et al., 2011) and oceanic (Xie et al., 2017) temperatures, and in sea ice concentrations (Comiso, 2017) (Appendix A11).

The Arctic climate has warmed significantly, and mean surface air temperatures were 0.4 to 2.3 °C higher during our survey period than in the preceding decade (Table 3). However, while atmospheric warming has occurred across the region as a whole, ocean warming and sea ice retreat have been largely restricted to sectors east of Greenland, where observations of ice stream formation (Zheng et al., 2019) and acceleration of ice flow (Strozzi et al., 2017b) show that GIC have experienced significantly increased glacier discharge (Fig. 4). For example, across the BKS sector, including Svalbard, Novaya Zemlya, Franz Josef Land, and Severnaya Zemlya, the average rise in sea surface, subsurface ocean, and atmospheric temperatures adjacent to GIC have been 0.8 °C, 0.5 °C, and 1.8 °C, respectively, and the average reduction in sea ice concentration has been 9.0 % (Table 3). By comparison, the ocean temperature and sea ice concentration around the Canadian Arctic Archipelagos have changed little.

Table 3

Anomalies in air surface temperature (T_{2m}), sea surface temperature (SST), subsurface ocean temperature (SOT), and sea ice concentration (SIC) during the survey period (2010-2017) relative to the previous decade (2000-2009). T_{2m} and SST are from ERA-Interim; SOT is 200m depth ocean temperature from TOPAZ; SIC data are from NASA bootstrap/team (Appendix A11).

Region	T_{2m} [°C]	SST [°C]	SOT [°C]	SIC [%]
FJL	+2.3	+0.3	+0.3	-13.2
NZ	+2.1	+0.9	+0.6	-8.2
SZ	+1.9	+0.2	+0.3	-7.6
Sv	+1.5	+1.1	+0.5	-8.4
Ic	+0.8	-0.1	+0.2	-0.1
CAA-N	+0.	+0.1	-0.3	-0.4
CAA-S	+1.3	+0.2	-0.3	-0.5
CAA	+0.9	+0.2	-0.3	-0.5
RAA	+2.1	+0.5	+0.4	-9.7
BKS	+1.8	+0.8	+0.5	-9.0

1

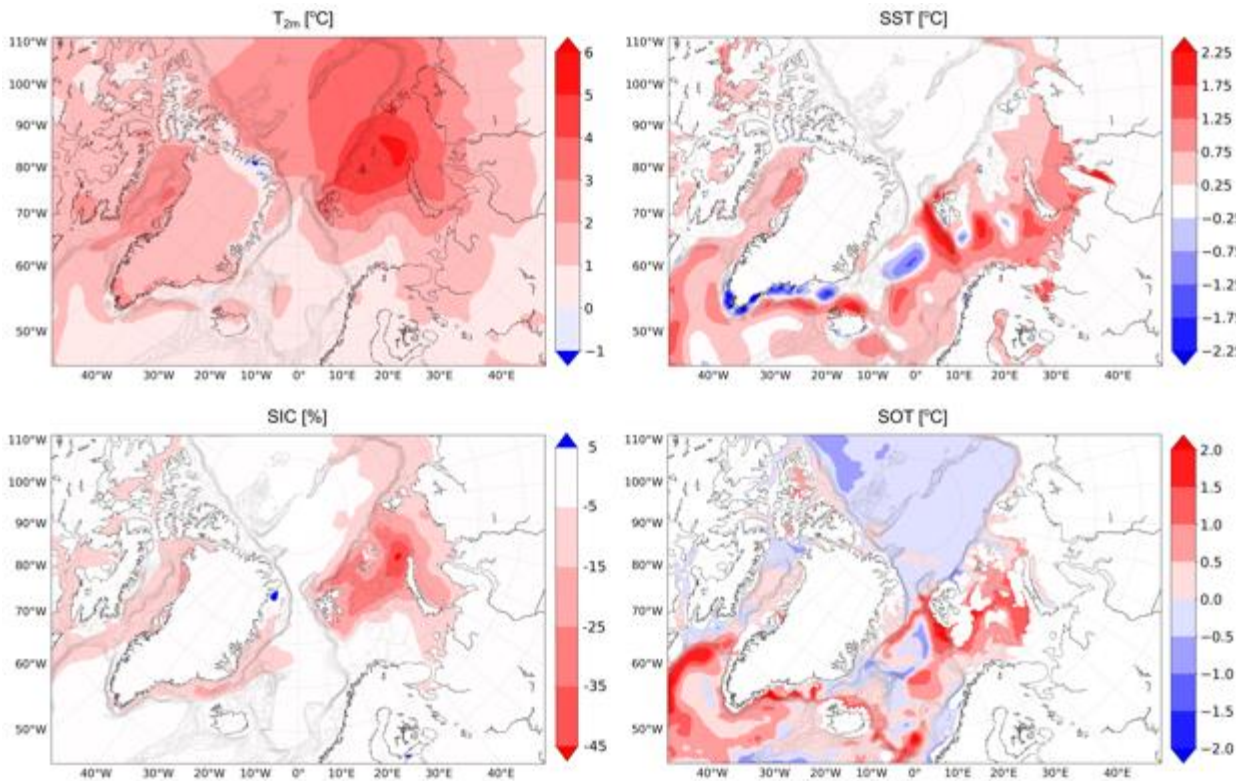


Fig. 4. Arctic climate forcing anomalies. Air surface temperature (T_{2m}), sea surface temperature (SST), subsurface ocean temperature (SOT), and sea ice concentration (SIC) anomalies during the CryoSat-2 period (2010-2017) with reference to the baseline period (1990-1999). T_{2m} and SST are from ERA-Interim, SOT is 200m depth ocean temperature from TOPAZ, and SIC are from the NASA Team sea ice algorithm. Anomalies with reference to the previous decade (2000-2009) are provided in Appendix D.

1 The warming of the BKS sector has been associated with the combined effects of
2 enhanced storm activity and increased Atlantic Water inflow to the Eurasian and Siberian Shelf
3 seas (Barton et al., 2018; Lind et al., 2018; Polyakov et al., 2017). Farther afield, it has also been
4 shown that the Arctic- and North Atlantic Oscillations are correlated with glacier mass balance
5 (Bjørk et al., 2018; Carr et al., 2017; Ding et al., 2014; Gardner and Sharp, 2006; Moholdt et al.,
6 2012b; Wouters et al., 2019; Zeeberg and Forman, 2001), with opposite effects in the eastern
7 and western Hemispheres depending on the position and strength of the Arctic Circumpolar
8 Vortex (Bjørk et al., 2018; Gardner and Sharp, 2006; Wouters et al., 2019). These modes of large-
9 scale atmospheric variability in the North Atlantic are likely to impact not only SMB via surface
10 warming but also trigger dynamic instabilities by affecting sea ice concentrations and ocean
11 warming in addition to changes in the atmosphere, albeit with possible delayed response times
12 and associated regional heterogeneity (Wouters et al., 2019).

13

14 **6. Conclusions**

15 Using CryoSat-2 swath radar altimetry, we have computed elevation and mass trends for all Arctic
16 GIC outside Greenland with unprecedented (500 m) spatial resolution. Between 2010 and 2017,
17 we estimate they have lost $87.0 \pm 2.6 \text{ Gt a}^{-1}$ of snow and ice on average, a 7% increase relative
18 to the 2003-2009 annual mean (Gardner et al., 2013) but with significant regional differences. By
19 modelling the contribution due to SMB, we isolate the elevation change signal due to anomalous
20 glacier flow. Using this approach, we find that SMB is responsible for the vast majority (87%) of
21 the observed mass loss, while ice discharge has caused the remainder (13%). However, based
22 on a significant number of independent observations, ice discharge from GIC in the Barents and
23 Kara Sea area has increased since the 2003-2009 period, and now accounts for 43% of the mass
24 loss from this region. This enhanced dynamic signal has been occurring in conjunction with
25 increased air and ocean temperature, and loss of sea ice (Morris et al., 2020).

1 It is predicted that, even when excluding tidewater glacier discharge, losses from the
2 Canadian Arctic Archipelagos and the BKS will be dominating glacier and ice cap mass loss
3 outside the Greenland and Antarctic Ice Sheets in future climate scenarios (Möller et al., 2016;
4 Radić et al., 2014). Most importantly, while SMB is projected to be the prevalent mechanism of
5 Greenland ice loss in the coming decades (Enderlin et al., 2014; Nick et al., 2013; Price et al.,
6 2011), a recent study finds that D, not SMB has dominated ice losses in Greenland over the past
7 half-century (Mouginot et al., 2019). Our results show that the dynamic response of marine-
8 terminating GIC to climate forcing makes up a significant proportion of the total mass budget in
9 the rest of the Arctic since 2010, with D contributing up to ten times the losses from SMB in some
10 regions, and with rapid and significant temporal fluctuations. This pattern is likely to endure over
11 time, as the large number of Arctic tidewater glaciers will continue to respond to receding sea ice
12 and to the impinging Atlantification of Arctic Ocean basins. We also emphasise the need for
13 caution when extrapolating in space and time observations of glacier changes from a limited
14 number of basins, and encourage the development and use of high-resolution, large-scale
15 observations of surface elevation, SMB, ice thickness and velocity to improve the quantitative
16 assessment of ice discharge. This is an essential step towards a more accurate representation of
17 dynamic imbalance in the parametrisation of climate models, and towards reducing uncertainty in
18 the projections of future ice mass loss in a changing climate.

19

20 **Acknowledgments**

21 This work was performed under the European Space Agency (ESA) Support to Science Elements
22 CryoSat+ CryoTop contract 4000107394/12/I-NB, CS+ Mountain Glaciers contract
23 4000114224/15/I-SBo to N.G. The authors would like to thank ESA for providing open access to
24 CryoSat-2 data, NASA for providing access to Operation Ice Bridge, and Dr. B.P.Y. Noël for
25 access to RACMO2.3 data.

26

1 **Appendix A. Methods**

2 **A1. Elevation data.** We use surface elevation data between 07/2010 and 07/2017 from the SAR
3 Interferometric Radar Altimeter (SIRAL) onboard the European Space Agency (ESA) CryoSat-2
4 satellite (Wingham et al., 2006). SIRAL is a beam-forming active microwave radar altimeter with
5 a maximum imaging range of ~15 km on the ground. The sensor emits time-limited *Ku-band*
6 pulses aimed at reducing the footprint to ~1.6 km within the beam. Over Arctic GIC, the sensor
7 operates in synthetic aperture interferometric (SARIn) mode, which allows delay-Doppler
8 processing to increase the along-track resolution to ~380 m, while cross-track interferometry is
9 used to extract key information about the position of the footprint center (Gray et al., 2015).
10 CryoSat-2 orbits the Earth with a 369-day repeat period formed by the successive shift of a 30-
11 day sub-cycle. The satellite has an inclination of 92°, offering complete coverage of the Arctic GIC
12 and a rapid increase in orbit cross-over density towards the poles - from 7.5 km inter-track
13 distance at the Equator to less than 1.6 km at latitudes higher than 70° (Gourmelen et al., 2018;
14 Wingham et al., 2006).

15
16 **A2. Swath processing.** We process *level 1b*, baseline C data supplied by the ESA ground
17 segment using a swath processing algorithm. *Level 1b* data is provided as a sequence of radar
18 echoes along the satellite track, which translates into single power, interferometric phase and
19 coherence waveforms for each along-track location (Gourmelen et al., 2018). The conventional
20 *level 1b* data processing method consists of extracting single elevation measurements from the
21 power signal in each waveform that corresponds to the Point of Closest Approach (POCA)
22 between satellite and the ground. In contrast, swath altimetry exploits the full radar waveform to
23 map a dense swath (~5km wide) of elevation measurements across the satellite ground track
24 beyond POCA (Christie et al., 2016; Foresta et al., 2016; Gourmelen et al., 2018; Gray et al.,
25 2013; Ignéczi et al., 2016) providing one to two orders of magnitude more elevation

1 measurements compared with POCA (Foresta et al., 2016; Gourmelen et al., 2018) (Appendix
2 E).

3
4 **A3. Gridded topography and elevation change.** Gridded elevation is computed using a plane-
5 fit algorithm for the entire measurement period, 2010-2017. The dense elevation field $h(x, y, t)$
6 allows gridding with a cell resolution of 500 m by 500 m to ensure sufficient spatial detail while
7 maximising the number of observations in each resolution cell (Foresta et al., 2016). The
8 measurements sampled within 500 m from each pixel center (x_p, y_p) are expressed as a function
9 of easting (x) , northing (y) , and time (t) :

$$10 \quad h(x, y, t) = c_0 x + c_1 y + c_2 t + c_3 = \nabla h(x, y) + \dot{h}t + c$$

11 with

$$12 \quad \nabla h(x, y) = \frac{\partial h}{\partial x} x + \frac{\partial h}{\partial y} y \quad \text{and} \quad \dot{h} = \frac{\partial h}{\partial t}$$

13 $\nabla h(x, y)$ is the ice surface gradient, and the time-dependent coefficient c_2 retrieved from
14 the linear fit is the rate of surface elevation change \dot{h} . The gridded elevations $h_p(x_p, y_p)$ are fitted
15 to the measurement field around each pixel center using an iterative 3σ -filter at each step until all
16 outliers are removed (Foresta et al., 2016).

17
18 **A4. Validation.** We compare CryoSat-2 gridded \dot{h} at 500 m posting with airborne records from
19 the NASA Operation Ice Bridge (OIB) Airborne Topographic Mapper (ATM). We were able to
20 locate two single validation test sites in the Arctic beyond Greenland with measurements sampled
21 after the launch of CryoSat-2: Barnes Ice Cap on Baffin Island, and Devon Ice Cap on Devon
22 Island, Canadian High Arctic. The data drawn for comparison is NASA IceBridge ATM L4 Surface
23 Elevation Rate of Change, Version1 (Studinger, 2014), sampled along extensive OIB repeat flight
24 paths in 2010 and 2015. We match these data with \dot{h} generated from CryoSat-2 measurements
25 acquired between 2010 and 2015. The validation is constrained to OIB measurements that are
26 within 250 m of the CryoSat-2 \dot{h} grid centre (1/2 grid spacing). We calculate a measurement bias

1 as the median value of the difference between swath products and OIB measurements (that is,
2 CryoSat-2 swath minus OIB). Validation of rates of \dot{h} yields a minimal bias of $0.05 \text{ m a}^{-1} \pm 0.26 \text{ m}$
3 a^{-1} and $0.00 \text{ m a}^{-1} \pm 0.13 \text{ m a}^{-1}$ respectively for Barnes and Devon Ice Caps (Appendix F). The
4 small difference can arise from differences in spatial and temporal resolution and/or signal
5 properties. We also inspected elevation time-series to ensure that rates of change were not
6 affected by spurious elevation biases related to changes in the scattering horizon (McMillan et al.,
7 2014; Nilsson et al., 2016). A more complete validation exercise of CryoSat-2 swath products was
8 performed by (Gourmelen et al., 2018) over parts of the Greenland- and Antarctic Ice Sheets.

9
10 **A5. Ice masks.** We use ice masks to delimit the regions covered in ice from bare ground and
11 ocean water in all gridded products. The masks are also used to differentiate between pixels
12 pertaining to land- *versus* marine-terminating basins. They are retrieved in vector (*shp*) format
13 from the Randolph Glacier Inventory (RGI) 6.0, available at Global Land Ice Measurements from
14 Space (GLIMS). Partitioning between land- and marine-terminating basins needed to be corrected
15 for misallocations in RGI 6.0 for some regions. Most substantial adjustments were made for
16 Svalbard, where a number of land-terminating basins needed to be re-allocated as marine-
17 terminating based on visual inspection of online maps from the Norwegian Polar Institute available
18 at www.npolar.no. Reallocation was made for the following GIC basins/ glaciers: Augnebreen,
19 Aldousbreen, Besselsbreen, Bragebreen, Deltabreen, Duckwitzbreen, Fjortende Julibreen,
20 Franklinbreen N and S, Frazerbreen, Gimlebreen, Hayesbreen, Hochstetterbreen, Idunbreen,
21 Infantfonna, Ingerbreen, Innifonna, Johansenbreen, Kongsbreen, Kongsvegen, Kronebreen,
22 Mittag-Lefflerbreen, Monacobreen, Negribreen, Nordenskiöldbreen, Nordssyselbreen,
23 Oslobreen, Paulabreen, Petermannbreen, Polarisbreen, Recherchebreen, Scheibreen,
24 Sidevegen, Spælbreen, Stonebreen, Tunabreen, Vaigattbreen.

25 The following Arctic sub-regions are covered by GIC but were not included in this study
26 as CryoSat-2 does not operate in SARIn mode at their location (see CryoSat-2 Geographical

1 Mode Mask, <https://earth.esa.int/web/guest/-/geographical-mode-mask-7107>, accessed on
 2 02/04/2019): Jan Mayen, Kvitøya Ice Cap (Sv), Victoria Ice Cap (FJL), Ushakov Ice Cap (Ushakov
 3 Island, RAA), Schmidt Ice Cap (SZ). Together these ice masses extend over a relatively small
 4 glaciated area (~1600 km²). The De Long Islands ice caps (East-Siberian Sea, RAA) were also
 5 excluded due to their small size (total glaciated area < 80 km² (Glazovskiy, 1996).
 6 For all regions, we assume that during the period of measurement the glaciated area remains
 7 constant. Information on imagery acquisition date, type of processing and source/ authorship is
 8 described in the GLIMS Technical Report 'Randolph Glacier Inventory – A Dataset of Global
 9 Glacier Outlines: Version 6.0' (https://www.glims.org/RGI/00_rgi60_TechnicalNote.pdf, accessed
 10 on 27/11/2020). For each of the regions defined in our study, this summarises as follows:
 11

CAAN	1999-2003 2000-2003	Landsat 7 (ETM+) ASTER
CAAS	1958/1982 2006-2010 1999-2002	Compiled from CanVec maps (Natural Ressources Canada) Aerial photographs SPOT5 Landsat 7 (ETM+)
Iceland	1999-2004	ASTER and SPOT5
Svalbard		Variety of sources and additions. Mainly SPOT5-HRS DEMs and orthoimages
RAA	2000-2010	Manually digitised from SPIRIT SPOT5 and Landsat imagery

12 **A6. Volume change.** We use surface elevation changes from our gridded \dot{h} maps to calculate
 13 volume change rates \dot{V} over the entire Arctic between 2010 and 2017. Volumetric changes are
 14 computed as the sum of the gridded surface elevation change rates from each pixel of a denoised
 15 gridded \dot{h} product multiplied by the pixel area as defined by the posting (0.5 x 0.5 km² per pixel):

$$16 \quad \dot{V}_{denoised} = A_{pixel} \cdot \sum \dot{h}_{denoised}$$

1 Denoising is performed for each region separately by removing pixels with values of $|\dot{h}| >$
 2 δ , and errors on \dot{h} above a certain threshold. We choose $\delta = 25 \text{ m a}^{-1}$ and $\delta = 50 \text{ m a}^{-1}$ for land-
 3 and marine-terminating basins, respectively, as the maximum realistic rates of change. Errors on
 4 \dot{h} are extracted from the covariance matrix of the plain-fit algorithm used to compute gridded
 5 elevations (Foresta et al., 2016). We select an appropriate error threshold by iteratively computing
 6 $\dot{V}_{denoised}$ while increasing the allowed maximum error on \dot{h} at each step until $\dot{V}_{denoised}$ converges
 7 towards a plateau value. The final error threshold is chosen so that the number of outliers is
 8 minimised after $\dot{V}_{denoised}$ converges. \dot{h} error thresholds vary between $3 \pm 2 \text{ m a}^{-1}$ and are specific
 9 for each region.

10 To calculate the total volume change \dot{V} , we make assumptions about areas not covered
 11 by measurements or where outliers were removed. For the land-terminating segments, where we
 12 assume that SMB processes are largely dominating the overall mass budget, we fill the data gaps
 13 by applying hypsometric averaging following the method used in (Foresta et al., 2016) (Appendix
 14 B). This approach is not applicable for marine-terminating basins however, where dynamic
 15 processes often lead to significant geometric changes over the ice surface, and hence, a simple
 16 relationship between \dot{h} and elevation is not sufficient to describe volume loss. Thanks to the high
 17 density of observations provided by CryoSat-2 (Appendix B), particularly for the marine-
 18 terminating sectors of Franz Josef Land, Novaya Zemlya, Severnaya Zemlya, and Svalbard, we
 19 rescale $\dot{V}_{denoised}$ using the ratio of total-to-measured glaciated area:

$$20 \quad \dot{V} = \frac{n_{total}}{n_{denoised}} \cdot \dot{V}_{denoised}$$

21 where n_{total} is the total number of pixels and $n_{denoised}$ the number of pixels in the denoised
 22 \dot{h} product. We performed a sensitivity test of the upscaling method by comparing against
 23 hypsometric averaging over the land-terminating segments of single CAA ice caps (Appendix B).
 24 Both CAA-N and CAA-S are characterised by rugged topography and are the regions with lowest
 25 data coverage. The comparison reveals little difference in the mass budget between the two

1 regionalisation schemes. We therefore apply upscaling as a method to fill data gaps in the marine-
2 terminating segments of all Arctic GIC, including CAA-S and CAA-N. Satellite coverage is typically
3 > 98 % and > 80 % of the total glaciated area in the BKS and the CAA, respectively (Appendices
4 C1-C6). Measured areas after removal of noise are given for each GIC in Appendix B. Spurious
5 elevation change samples are randomly distributed across the GIC area. In some cases where
6 the topography at the ice cap margin is particularly steep, spurious measurements tend to
7 concentrate at low elevation, where thinning is accentuated (Appendices C1-C6). We therefore
8 infer that our estimates of ice loss from marine-terminating GIC segments, where upscaling of
9 volume change is applied, are rather on the conservative side.

10
11 **A7. Mass change.** The conversion from volume- to mass change is performed using a constant
12 density of ice ρ_{ice} equal to $850 \pm 60 \text{ kg m}^{-3}$ as advocated by (Huss, 2013) to better account for a
13 wide range of surface conditions. For each of the seven regions in Table 1 we apply the
14 appropriate regionalisation scheme to the sum of all land- and marine-terminating basins
15 separately, and compute the corresponding land- and marine-terminating mass budgets (\dot{m}_l and
16 \dot{m}_m , respectively) (Appendix B). The total mass balance \dot{m} is then calculated as the sum of the
17 two segments:

$$\dot{m} = \dot{m}_l + \dot{m}_m$$

18
19 Computing mass budgets on a single ice cap basis brings insignificant changes to the
20 overall result (Appendix B), with differences well within error margins. For the CAA, this confirms
21 similar findings by (Gardner et al., 2011). Specific mass balance is calculated as the ratio of mass
22 change to surface area, whereby the glaciated area extent is based on the glacier outlines from
23 RGI 6.0.

24
25 **A8. Partitioning total mass balance into SMB and D.** Local elevation changes over the ice
26 surface occur as a result of surface mass balance (SMB) anomalies and the advection of ice

1 masses (D) and are described by the kinematic relation for \dot{h} (e.g. Cuffey and Paterson, 2010).
 2 To quantify the relative contribution of SMB and D to the overall mass loss we parametrise
 3 elevation change (\dot{h}_l) as a function of elevation (h_l) and spatial coordinates (x_l, y_l) over the sum
 4 of all land-terminating GIC basins only, for each of the seven regions listed in Table 1:

$$5 \quad \dot{h}_l \approx a_0 h_l^3 + a_1 h_l^2 + a_2 h_l + a_3 x_l + a_4 y_l + a_5$$

6 The function describes the direct influence of elevation, latitude and longitude on SMB-
 7 related elevation change \dot{h}_l . We use the coefficients a_i (Appendix G) and gridded elevations h_l
 8 (x_l, y_l, t) and h_m (x_m, y_m, t) over land- and marine-terminating sectors, respectively, to calculate
 9 parametrised \dot{h}_{p_l} and \dot{h}_{p_m} , separately for both types of basins. We derive bulk marine-terminating
 10 SMB_m as follows:

$$11 \quad SMB_m = SMB_l \cdot \sum_{n_m} \dot{h}_{p_m} / \sum_{n_l} \dot{h}_{p_l}$$

12 where SMB_l is equal to the total mass balance \dot{m}_l of land-terminating GIC basins
 13 (Appendix A7), and n_l and n_m are the number of pixels in the gridded \dot{h}_{p_l} and \dot{h}_{p_m} maps,
 14 respectively. We then calculate D by subtracting SMB_m from the total mass balance \dot{m}_m of
 15 marine-terminating GIC basins. To evaluate our parametrisation of \dot{h}_l we calculate the root mean
 16 square error (RMSE) of the polynomial fit as:

$$17 \quad RMSE = \sqrt{\frac{\sum(\dot{h}_{p_l} - \dot{h}_l)^2}{n}}$$

18 where n is the number of grid cells. RMSE values vary regionally and range between 0.53
 19 m a^{-1} and 6.41 m a^{-1} .

20 **A9. SMB comparison CryoSat-2 - RACMO2.3.** To evaluate our method for partitioning mass
 21 imbalance into SMB and D, we use seven glaciological years (10/2010 - 09/2017) of monthly
 22 area-specific SMB data for CAA-N and CAA-S from the Regional Climate Model RACMO2.3. The
 23 dataset and the corresponding ice masks are down-sampled to 1km (Noël et al., 2018). We

1 produce additional ice masks at 1km resolution for marine- and land-terminating basins separately
 2 for both CAA-N and CAA-S based on the RGI 6.0 split between the two types of basins. Annual
 3 SMB is calculated pixelwise for each year and then integrated over the entire area to obtain total
 4 SMB by region and terminus type.

5 Over Svalbard, parametrised SMB ($-7.1 \pm 0.6 \text{ Gt a}^{-1}$) compares well with reconciled 2010-
 6 2019 estimates from Schuler et al. (2020) ($-8 \pm 2 \text{ Gt a}^{-1}$) (Table A1), although there is a large
 7 difference in the estimated discharge D between the two approaches. Nevertheless, Schuler et
 8 al.'s estimated dynamic imbalance ($-2 \pm 6 \text{ Gt a}^{-1}$) is based on two years of additional data, and it
 9 is calculated as the residual between total geodetic mass balance and modelled SMB, with a large
 10 associated uncertainty of $\pm 6 \text{ Gt a}^{-1}$, which keeps this estimate within error compared with our
 11 discharge estimate derived from CryoSat-2 ($-6.2 \pm 0.9 \text{ Gt a}^{-1}$) (Table A1). The latter is also in
 12 excellent agreement with calving rates from Blaszczyk et al. (2009) ($-6.1 \pm 1.5 \text{ Gt a}^{-1}$) (Table A1),
 13 which to date is the only available study to have quantified frontal ablation of Svalbard's glaciers
 14 and ice caps (Schuler et al., 2020). However, given the large increase in dynamic ice loss from
 15 Svalbard's tidewater glaciers during the 2010s (Schuler et al., 2020), this comparison suggests
 16 that either Blaszczyk et al.'s 2000-2006 estimate was overestimated, or bulk D derived from the
 17 CryoSat-2 SMB parametrisation is underestimated.

18

19 **Table A1.** SMB and D from various sources.

20

Units [Gt a^{-1}]	MT MB	LT SMB	Total SMB	D	Total MB
CryoSat-2 (2010-2017)	-4.6 ± 0.5	-2.5 ± 0.3	-7.1 ± 0.6	-6.2 ± 0.9	-13.3 ± 0.8
van Pelt et al. (2019) (2010-2017)	$-0.4 \pm \sigma$	$-1.4 \pm \sigma$	$-1.8 \pm \sigma$	-6.1 ± 1.5	$-7.9 \pm \sigma$
Schuler et al. (2020) (2010-2019)	-	-	-8 ± 2	-2 ± 6	-10 ± 4
Blaszczyk (2009) (2000-2006)	-	-	-	-6.1 ± 1.5	-

21

22

23

24 **A10. Errors.** The uncertainty associated with the calculated mass imbalance is the result of
 25 unknown density fluctuations, gradients in snow accumulation, and errors in elevation trends from

1 the satellite measurements. The elevation measurement errors can be attributed to instrument
 2 system errors (intrinsic to *Level 1b* data) on one hand, and to sampling errors in the swath
 3 processing algorithm on the other hand. We estimate a representative uncertainty of the mass
 4 imbalance, using the same method as in (Foresta et al., 2016). We account for errors in the
 5 measurement statistically by extracting from the covariance matrix of our surface elevation fit the
 6 variances $\varepsilon_{\dot{h}}$ that are assigned to the rates of \dot{h} (Foresta et al., 2016). Depending on the type of
 7 drainage basin, the error on volume change $\varepsilon_{\dot{V}}$ is obtained by propagating $\varepsilon_{\dot{h}}$ either by
 8 hypsometric averaging (land-terminating basins), or rescaling by the ratio of total-to-measured
 9 surface area (marine-terminating basins). For the volume-to-mass conversion we assume a
 10 constant error on the density $\varepsilon_{\rho} = 60 \text{ kg m}^{-3}$ following Huss (2013). The error on the mass
 11 imbalance is calculated using uncorrelated Gaussian error propagation as:

$$12 \quad \varepsilon_{\dot{m}} = |\dot{m}| \cdot \sqrt{\left(\frac{\varepsilon_{\dot{V}}}{\dot{V}}\right)^2 + \left(\frac{\varepsilon_{\rho}}{\rho_{ice}}\right)^2}$$

13 For land-terminating drainage basins we assume that $\varepsilon_{\dot{m}} = \varepsilon_{SMB}$. SMB uncertainties of
 14 marine-terminating basins are estimated by assigning the root mean square deviation of our SMB
 15 parametrisation to the error $\varepsilon_{\dot{h}}$ on \dot{h} and applying Gaussian error propagation as described above.
 16 For D we derive uncertainties ε_D from the quadrature of $\varepsilon_{\dot{m}}$ and ε_{SMB} :

$$17 \quad \varepsilon_D = \sqrt{(\varepsilon_{\dot{m}})^2 + (\varepsilon_{SMB})^2}$$

18 Satellite coverage and valid measurement samples are sufficient to be representative of
 19 the overall mass balance of marine-terminating GIC basins, which justifies the applicability of the
 20 upscaling method. Undersampling at low elevation, where dynamic thinning prevails, may lead to
 21 an underestimation of the losses in certain marine-terminating basins (Appendix A6). This is not
 22 accounted for as a source of uncertainty in this study.

23 Ice masks are largely based on satellite imagery from the 2000s, although data sources
 24 and time of acquisition used for glacier delineation vary by region (Appendix A5). The time lag

1 between CryoSat-2 measurements and glacier outlines thus forms a potential source of error in
2 our nominal mass balance estimates, in particular in regions where frontal advance and retreat of
3 glacier termini have been significant over the past two decades, such as in Svalbard and Novaya
4 Zemlya. However, glacier advance and retreat are small compared to the total glaciated area of
5 Arctic GIC, and hence we imply that the related uncertainty remains small at the pan-Arctic scale.
6 Furthermore, when comparing our estimates with those of previous studies using the same glacier
7 outlines, such as Gardner et al. (2013) for example (Table 1), this error source is reduced in terms
8 of the area-specific mass budgets.

9 In regions characterised by strong dynamical thinning, surface elevation changes result in
10 a redistribution of the ice masses beyond the applied glacier delimitations. We note that such
11 redistribution only affects a small number of marine-terminating basins, such as Basin 3
12 (Austfonna Cap) and the Vavilov Ice Cap, where accumulation of ice is occurring offshore, and
13 hence not affecting sea level change. It is beyond the scope of this paper to account for these
14 processes quantitatively for each region. However, we expect uncertainties related to ice
15 advection outside of the defined glacier area to potentially impact estimates of sea-level
16 contribution increasingly in the future in the absence of regular updates of the RGI glacier
17 inventories.

18 There is significant difference in the range of uncertainties associated with derived SMB
19 from CryoSat-2 and RACMO2.3 (Figure 2b). The large uncertainties in the RACMO2.3 model
20 result from large biases between modelled data and observations, while uncertainties in the
21 CryoSat-2 parametrisation may be underestimated by the assumption that all 500 x 500 m
22 samples are independent. In reality, SMB patterns may be correlated over distances of several
23 kilometers depending on the region (e.g. Moholdt, 2010; Rolstad et al., 2009), which reduces the
24 number of independent samples and increases the error. This effect is difficult to quantify in the
25 error budget in the absence of knowledge about the correlation distance at the regional scale.

26

1 **A11. Climate forcing.** We use maps of monthly mean SST and T_{2m} on a $0.75^\circ \times 0.75^\circ$ grid and
2 averaged into monthly means from ECMWF Interim Reanalysis (ERA-I) (Dee et al., 2011), with
3 the smallest bias from observations (Lindsay et al., 2014). We extract 200 m depth SOT from the
4 Arctic Ocean reanalysis TOPAZ (Xie et al., 2017) on a 12-16 km grid, and analysed for the 15th
5 day of each month. The passive microwave NASA Team (Cavalieri et al., 2019) and Bootstrap
6 (Comiso, 2017) SIC data are monthly means on a 25 km by 25 km polar stereographic grid.
7 Regional averages surrounding each GIC (values in Table 3) are calculated by nearest neighbor
8 interpolation from the native grids of each forcing over the target regions in Figure 1.

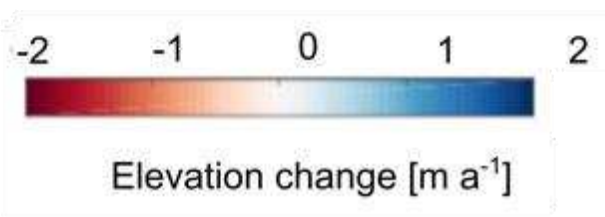
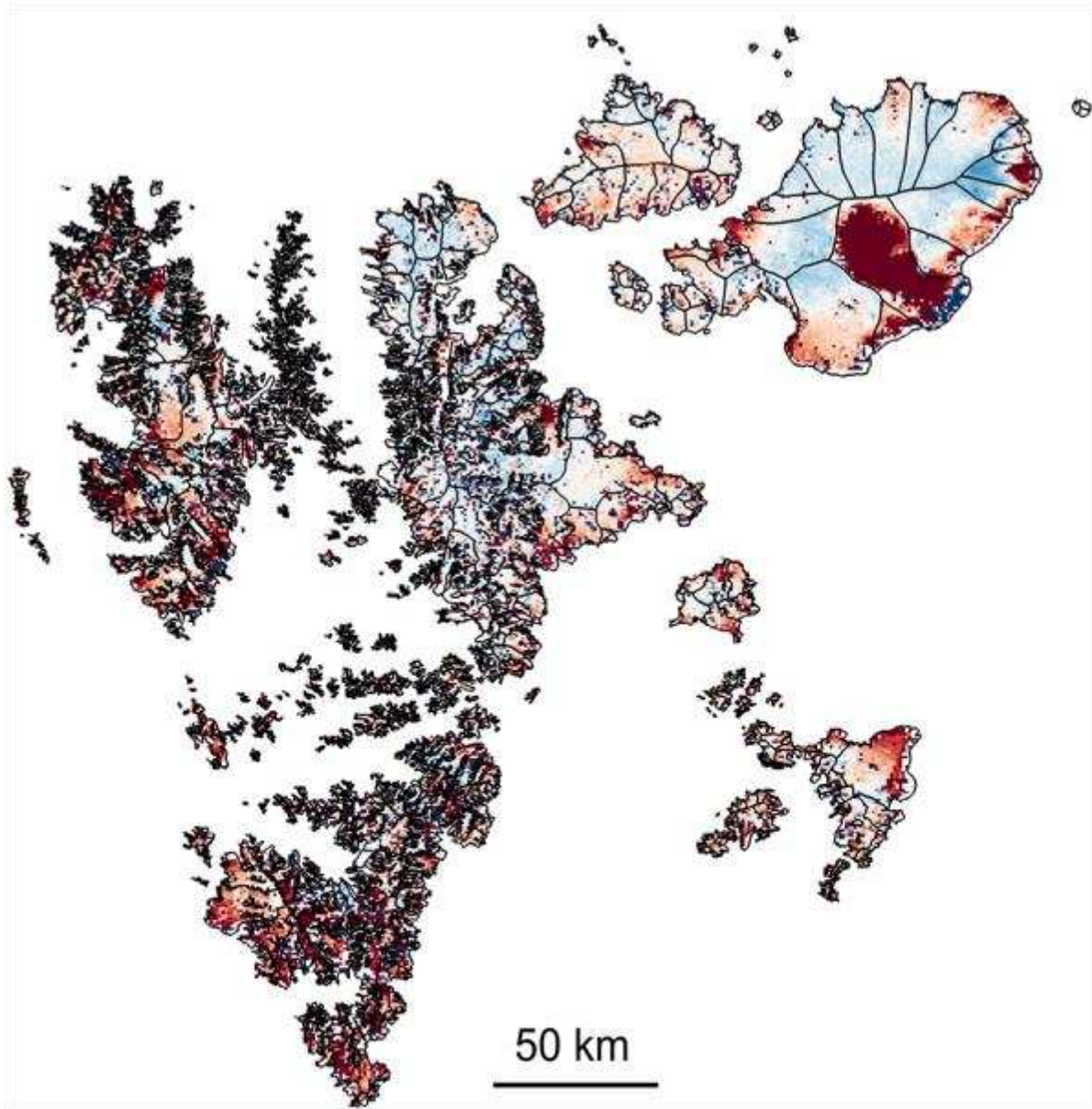
9
10 **A12. Data availability.** Our swath processing algorithm uses SARIn-mode CryoSat-2 *Level 1b*
11 format data directly downloaded from <ftp://science-pds.cryosat.esa.int> (accessed on 27/06/2019);
12 NASA Operation Ice Bridge validation data is available for download at
13 <https://nsidc.org/data/icebridge> (accessed on 27/06/2019); ice masks for all regions except
14 Iceland were taken from https://www.glims.org/RGI/rqi60_dl.html (accessed on 27/06/2019);
15 RACMO data is available for download at <https://doi.pangaea.de/10.1594/PANGAEA.881315>; the
16 passive microwave NASA Team and Bootstrap concentration data are available respectively
17 from <http://nsidc.org/data/nsidc-0051> and <http://nsidc.org/data/nsidc-0079>; The
18 ARCTIC_REANALYSIS_PHYS_002_003 TOPAZ product is available from
19 <http://marine.copernicus.eu/services-portfolio/access-to-products>; ERA-Interim monthly means of
20 daily means are available from <https://apps.ecmwf.int/datasets/>.

21

Appendix B. Mass balance of Arctic GIC. Split by type of basin (marine- and land-terminating), comparison of upscaling (S) *versus* hypsometric averaging (H) as regionalisation schemes of land-terminating basins. A_{measured} refers to glaciated area after removal of noise.

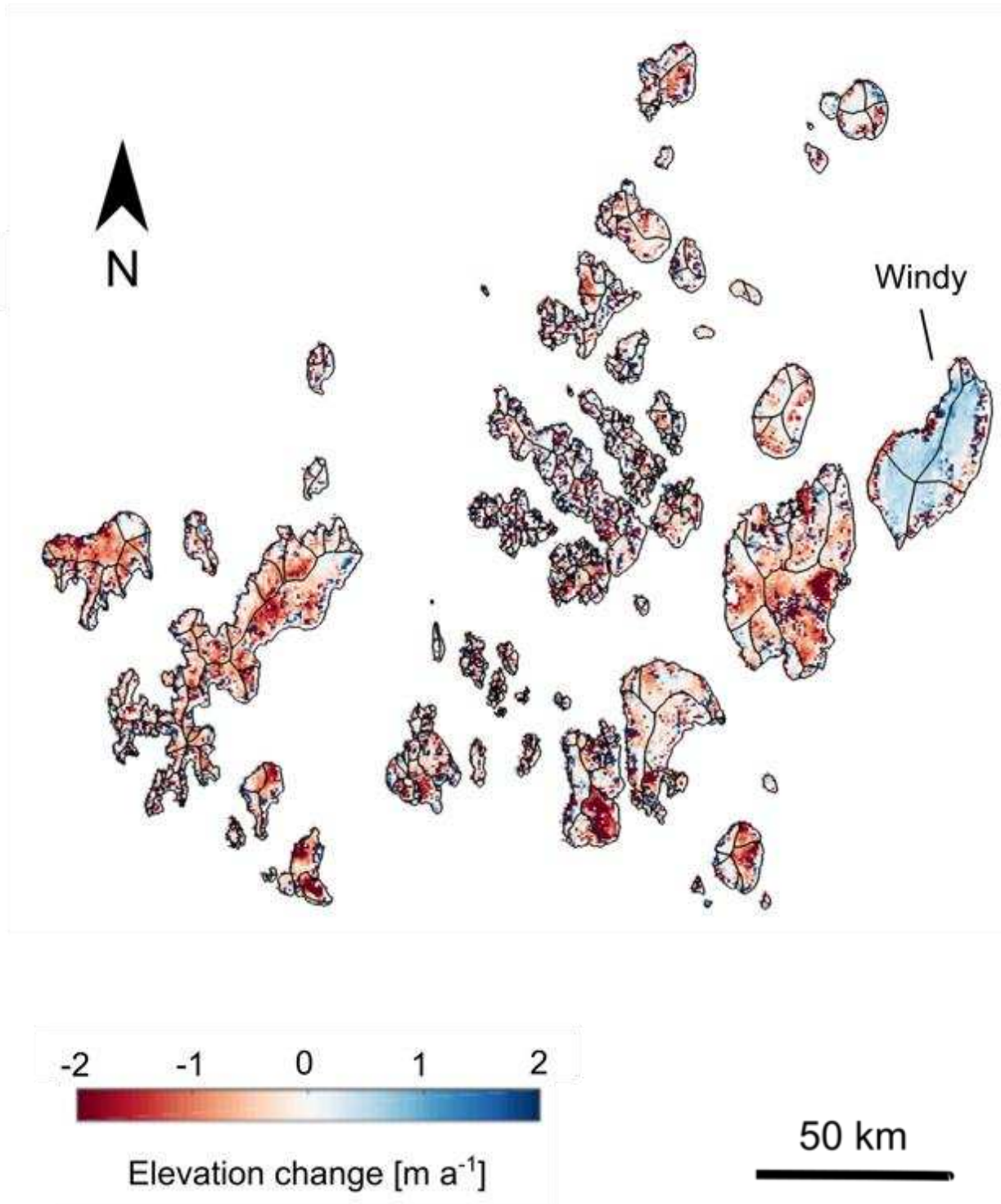
Region / GIC	Total MB	Marine-terminating basins		Land-terminating basins		
	[Gt a ⁻¹]	S [Gt a ⁻¹]	$A_{\text{measured}} / A_{\text{total}}$	S [Gt a ⁻¹]	H [Gt a ⁻¹]	$A_{\text{measured}} / A_{\text{total}}$
FJL	-3.8 ± 0.3	-3.7 ± 0.3	90%	-0.2 ± 0.0	-0.1 ± 0.0	88%
Windy	+0.3 ± 0.0	+0.2 ± 0.0	86%	+0.1 ± 0.0	+0.1 ± 0.0	82%
NZ	-8.5 ± 0.4	-5.2 ± 0.4	83%	-3.0 ± 0.2	-3.3 ± 0.2	70%
SZ	-1.7 ± 0.1	-1.6 ± 0.1	90%	0.1 ± 0.0	-0.1 ± 0.0	82%
Sum GIC and upscale	-1.7 ± 0.1	-1.6 ± 0.1		0.1 ± 0.0	-0.1 ± 0.0	
Academy of Sciences	-1.0 ± 0.1	-1.1 ± 0.1	94%	+0.1 ± 0.0	+0.1 ± 0.0	95%
Vavilov	-0.2 ± 0.0	-0.3 ± 0.0	94%	+0.1 ± 0.0	+0.1 ± 0.0	87%
Albanov	0.0 ± 0.0	0.0 ± 0.0		0.0 ± 0.0	0.0 ± 0.0	83%
Pioneer	0.0 ± 0.0	0.0 ± 0.0		0.0 ± 0.0	0.0 ± 0.0	82%
Rusanov	-0.2 ± 0.0	-0.1 ± 0.0	87%	-0.1 ± 0.0	-0.1 ± 0.0	76%
Karpinsky	-0.1 ± 0.0	-0.2 ± 0.0	84%	+0.1 ± 0.0	+0.1 ± 0.0	79%
University	+0.1 ± 0.0	0.0 ± 0.0	87%	+0.1 ± 0.0	+0.1 ± 0.0	85%
Semenov-Tyan-Shansky + Kropotkin + Leningradsky	-0.2 ± 0.0	0.0 ± 0.0	75%	-0.2 ± 0.0	-0.2 ± 0.0	76%
Sv	-13.3 ± 0.8	-10.8 ± 0.8	85%	-2.5 ± 0.2	-2.5 ± 0.2	69%
Sum GIC and upscale	-13.8 ± 0.4	-11.2 ± 0.4		-2.6 ± 0.1	-2.6 ± 0.1	
Austfonna	-4.6 ± 0.3	-4.6 ± 0.3	98%	0.0 ± 0.0	0.0 ± 0.0	89%
Vestfonna	-0.4 ± 0.0	-0.4 ± 0.0	95%	0.0 ± 0.0	0.0 ± 0.0	90%
Barentsøya	-0.2 ± 0.0	-0.1 ± 0.0	92%	-0.1 ± 0.0	-0.1 ± 0.0	90%
Edgeøya	-0.9 ± 0.0	-0.5 ± 0.0	90%	-0.4 ± 0.0	-0.4 ± 0.0	84%
NW Spitzbergen	-2.7 ± 0.1	-1.9 ± 0.1	77%	-0.8 ± 0.1	-0.8 ± 0.1	58%
NE Spitzbergen	-0.7 ± 0.0	-0.4 ± 0.0	82%	-0.3 ± 0.0	-0.3 ± 0.0	67%
S Spitzbergen	-4.0 ± 0.2	-3.1 ± 0.2	74%	-0.8 ± 0.1	-0.9 ± 0.1	67%
Ic	-2.6 ± 0.2			-1.2 ± 0.1	-2.6 ± 0.2	80%
Sum GIC and upscale	-2.6 ± 0.1			-1.4 ± 0.1	-2.6 ± 0.1	
Vatnajökull	-1.6 ± 0.1			-0.9 ± 0.1	-1.6 ± 0.1	84%
Langjökull	-0.3 ± 0.0			-0.3 ± 0.0	-0.3 ± 0.0	77%
Hofsjökull	-0.2 ± 0.0			-0.1 ± 0.0	-0.2 ± 0.0	84%
Mýrdalsjökull + Eyafjallajökull	-0.1 ± 0.0			+0.1 ± 0.0	-0.1 ± 0.0	63%
Drangajökull	-0.1 ± 0.0			+0.1 ± 0.0	-0.1 ± 0.0	67%
CAA-N	-32.3 ± 1.6	-13.3 ± 0.9	63%	-17.9 ± 1.3	-19.0 ± 1.3	62%
Sum GIC and upscale	-32.6 ± 0.8	-12.9 ± 0.4		-18.0 ± 0.6	-19.7 ± 0.6	
N Ellesmere	-9.4 ± 0.5	-2.7 ± 0.2	56%	-6.0 ± 0.4	-6.7 ± 0.5	57%
Agassiz	-5.0 ± 0.3	-1.5 ± 0.1	52%	-3.1 ± 0.2	-3.5 ± 0.3	64%
Muller	-2.8 ± 0.2	-0.2 ± 0.0	41%	-2.4 ± 0.2	-2.6 ± 0.2	59%
Steacie	-1.8 ± 0.1			-1.6 ± 0.1	-1.8 ± 0.1	50%
Prince of Wales	-5.9 ± 0.3	-4.1 ± 0.3	61%	-1.7 ± 0.1	-1.8 ± 0.1	62%
Sydkap	-0.8 ± 0.0	-0.2 ± 0.0	55%	-0.6 ± 0.0	-0.6 ± 0.0	71%
Manson	-1.7 ± 0.1	-1.4 ± 0.1	71%	-0.3 ± 0.0	-0.3 ± 0.0	53%
Devon	-4.3 ± 0.2	-2.9 ± 0.2	83%	-1.3 ± 0.1	-1.4 ± 0.1	82%
CAA-S	-24.8 ± 1.8	-1.3 ± 0.1	37%	-23.1 ± 1.6	-23.5 ± 1.8	56%
Sum GIC and upscale	-24.5 ± 0.7	-1.5 ± 0.1		-22.7 ± 0.7	-23.0 ± 0.7	
Bylot	-2.3 ± 0.2	-0.2 ± 0.0	67%	-2.2 ± 0.2	-2.1 ± 0.2	54%
Barnes	-4.5 ± 0.3			-4.5 ± 0.3	-4.5 ± 0.3	97%
Penny	-4.3 ± 0.3	-0.8 ± 0.1	11%	-3.5 ± 0.2	-3.5 ± 0.3	44%
N Baffin	-2.3 ± 0.2	-0.2 ± 0.0	39%	-2.0 ± 0.1	-2.1 ± 0.2	51%
Central Baffin	-5.2 ± 0.4	-0.2 ± 0.0	50%	-4.8 ± 0.3	-5.0 ± 0.4	50%
S Baffin	-3.8 ± 0.3			-3.7 ± 0.3	-3.8 ± 0.3	42%
CAA	-57.1 ± 2.4	-14.5 ± 0.9	61%	-41.0 ± 2.1	-42.6 ± 2.2	60%
RAA	-14.0 ± 0.5	-10.5 ± 0.5	87%	-3.1 ± 0.2	-3.5 ± 0.2	77%
BKS	-27.3 ± 0.9	-21.3 ± 0.9	86%	-5.6 ± 0.3	-6.0 ± 0.3	73%
Total Arctic	-87.0 ± 2.6	-35.8 ± 1.3	74%	-47.8 ± 2.1	-51.2 ± 2.3	64%

1 **Appendix C1.** Surface elevation change rates (2010-2017) over Svalbard at 500 x 500 m
2 resolution. Spurious elevation changes removed during the post-processing stage are included in
3 the map.
4
5



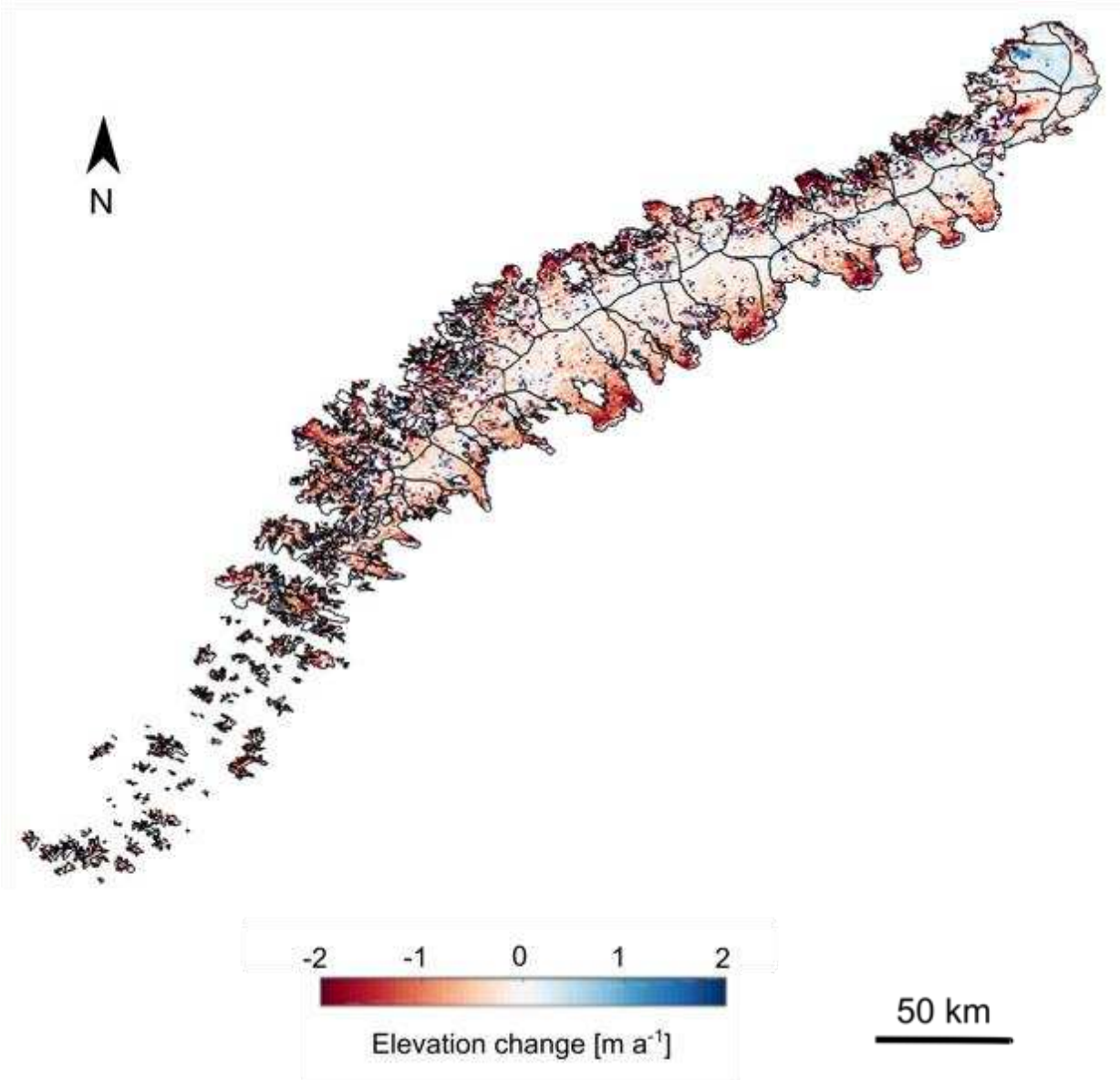
6

1 **Appendix C2.** Surface elevation change rates (2010-2017) over Franz Josef Land at 500 x 500
2 m resolution. Spurious elevation changes removed during the post-processing stage are included
3 in the map.
4
5
6



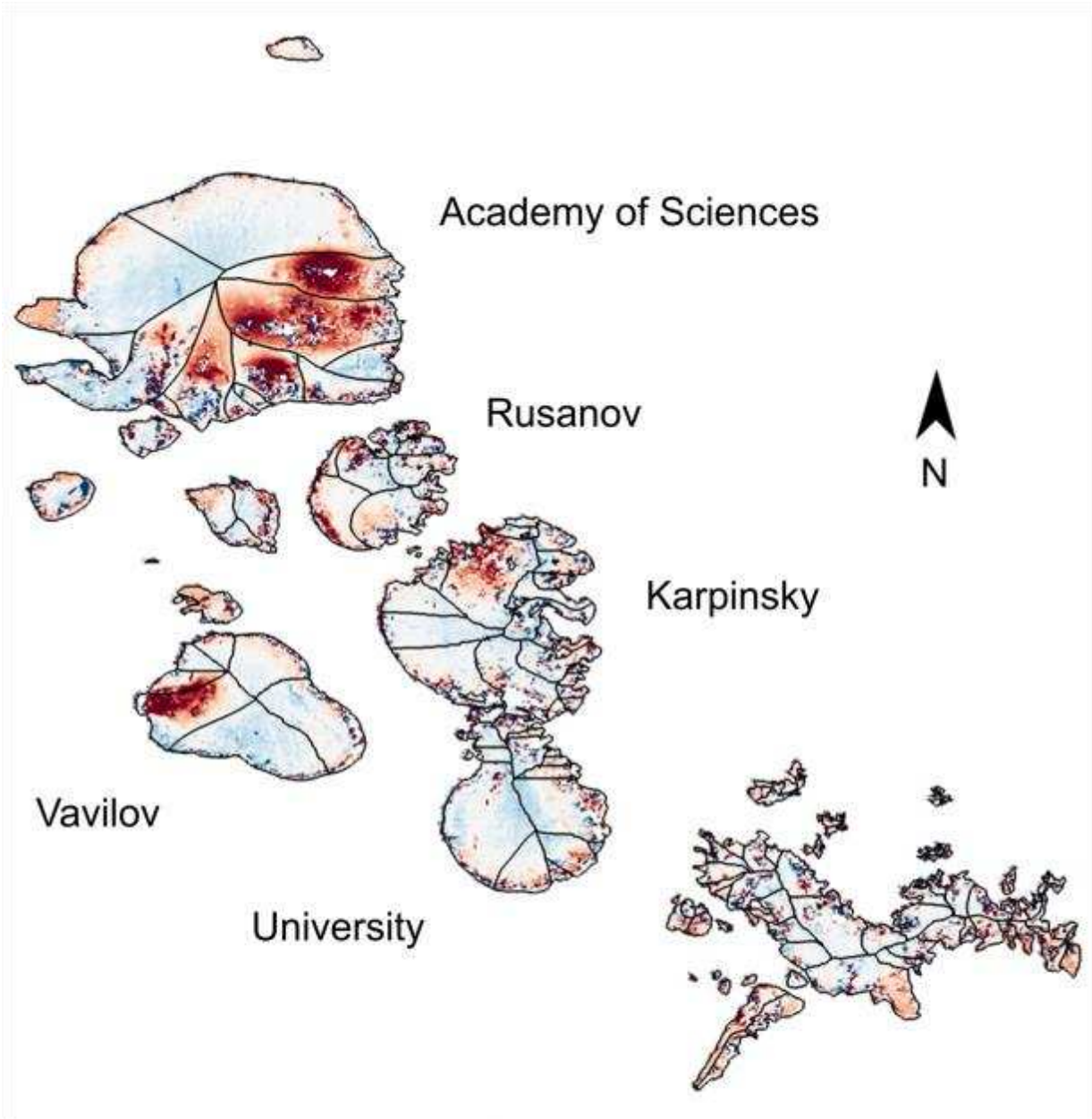
7
8

1 **Appendix C3.** Surface elevation change rates (2010-2017) over Novaya Zemlya at 500 x 500 m
2 resolution. Spurious elevation changes removed during the post-processing stage are included in
3 the map.
4
5
6
7
8



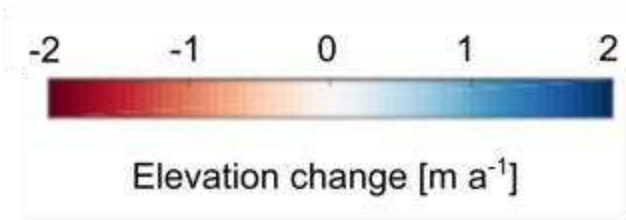
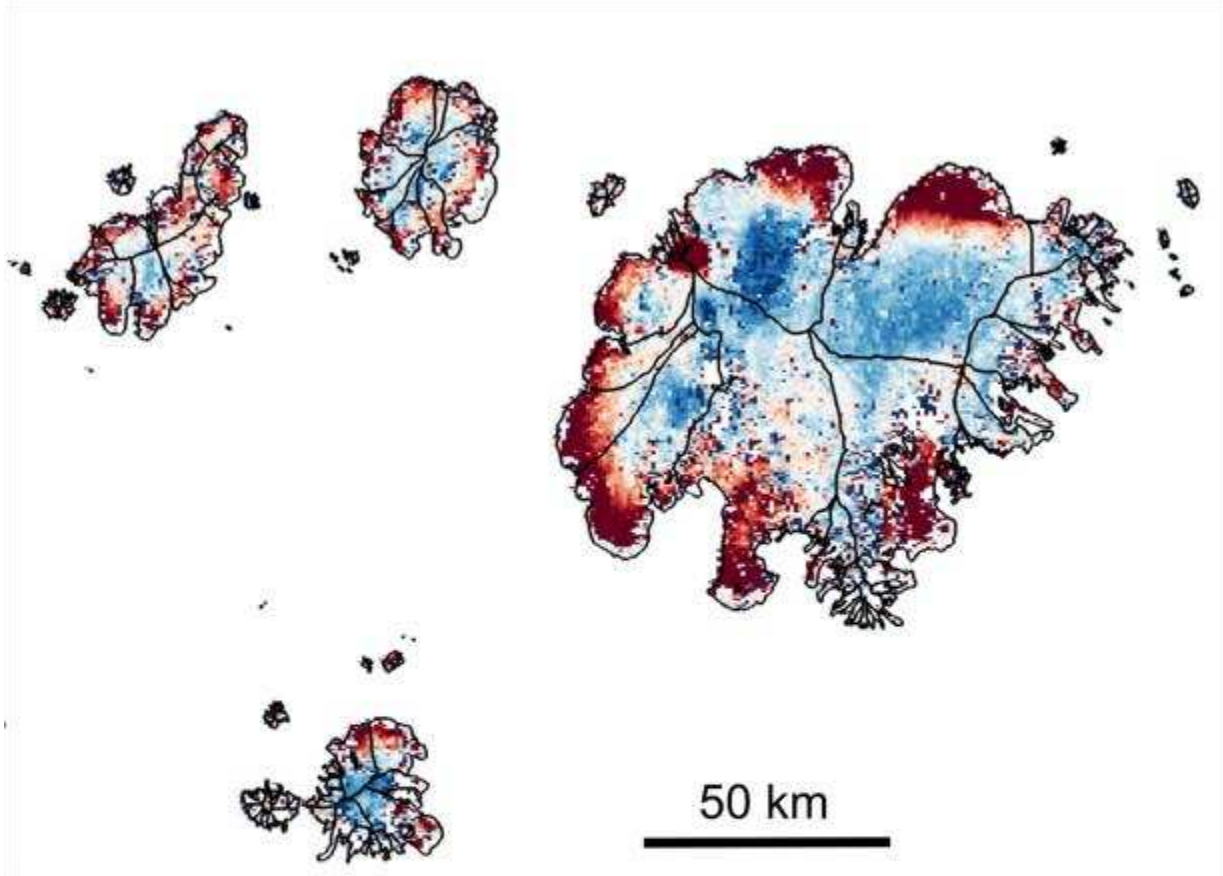
9
10

1 **Appendix C4.** Surface elevation change rates (2010-2017) over Severnaya Zemlya at 500 x 500
2 m resolution. Spurious elevation changes removed during the post-processing stage are included
3 in the map.
4
5



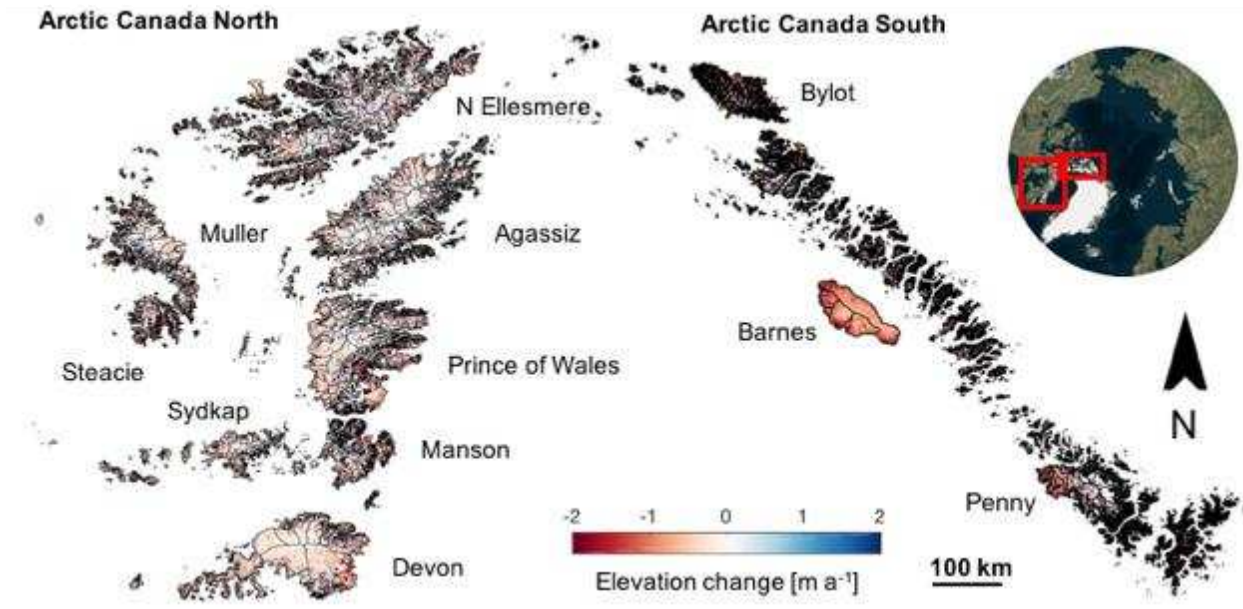
6

1 **Appendix C5.** Surface elevation change rates (2010-2017) over Iceland at 500 x 500 m
2 resolution. Spurious elevation changes removed during the post-processing stage are included in
3 the map.
4
5
6
7



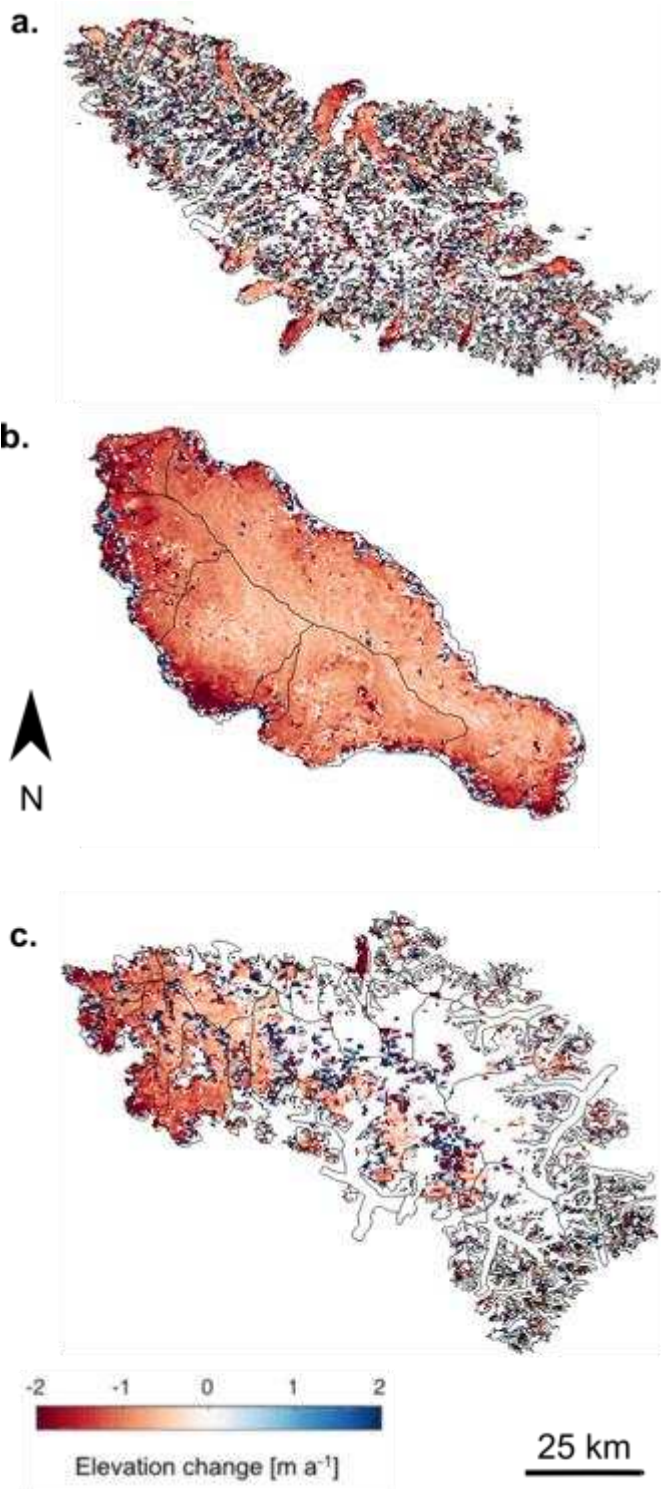
8

1 **Appendix C6a.** Surface elevation change rates (2010-2017) over the Canadian Arctic
2 Archipelagos at 500 x 500 m resolution. Spurious elevation changes removed during the post-
3 processing stage are included in the map.
4
5
6



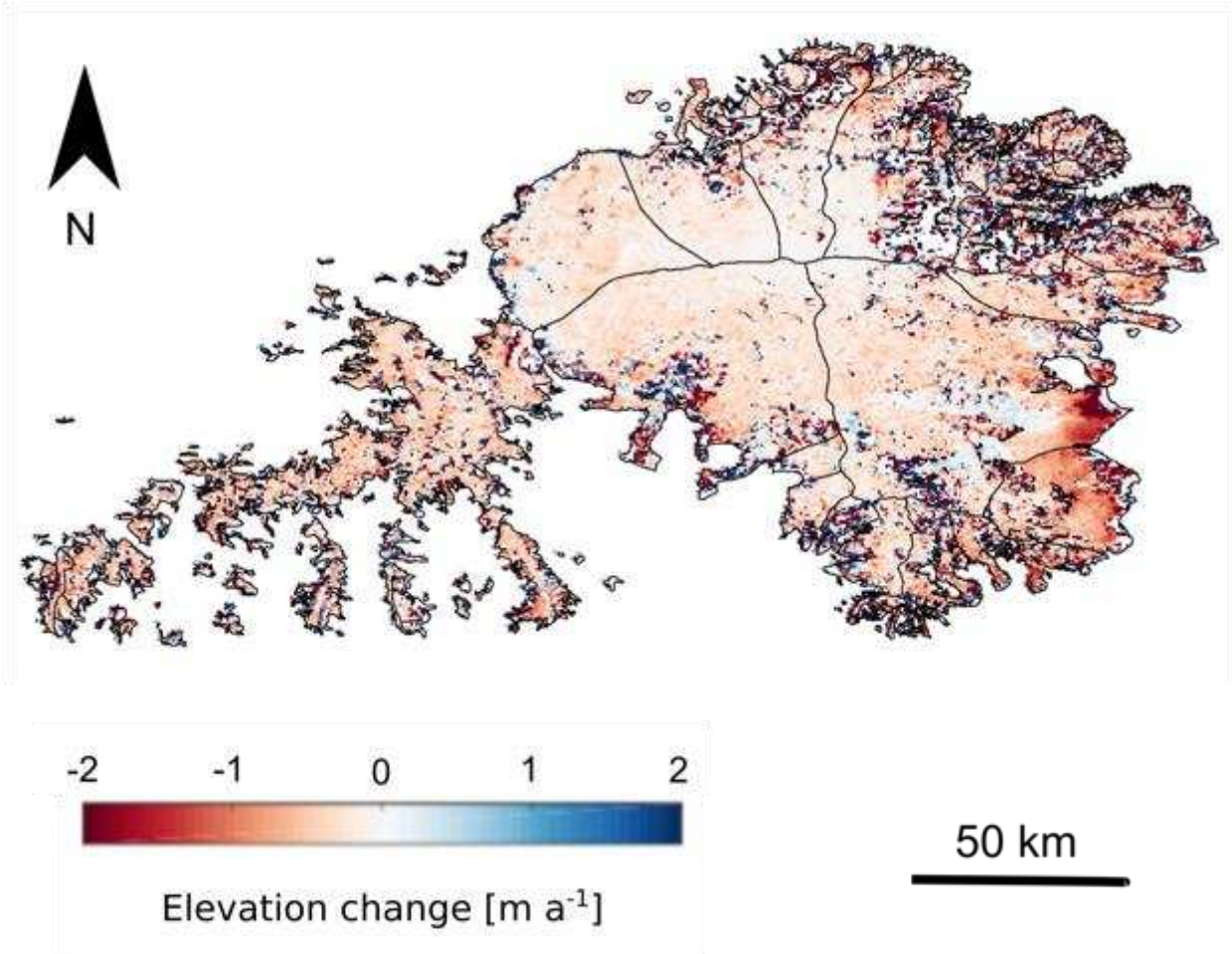
7
8
9
10

1 **Appendix C6b.** Surface elevation change rates (2010-2017) over (a) Bylot Island, (b) Barnes Ice
2 Cap, and (c) Penny Ice Cap, at 500 x 500 m resolution. Spurious elevation changes removed
3 during the post-processing stage are included in the map.
4
5



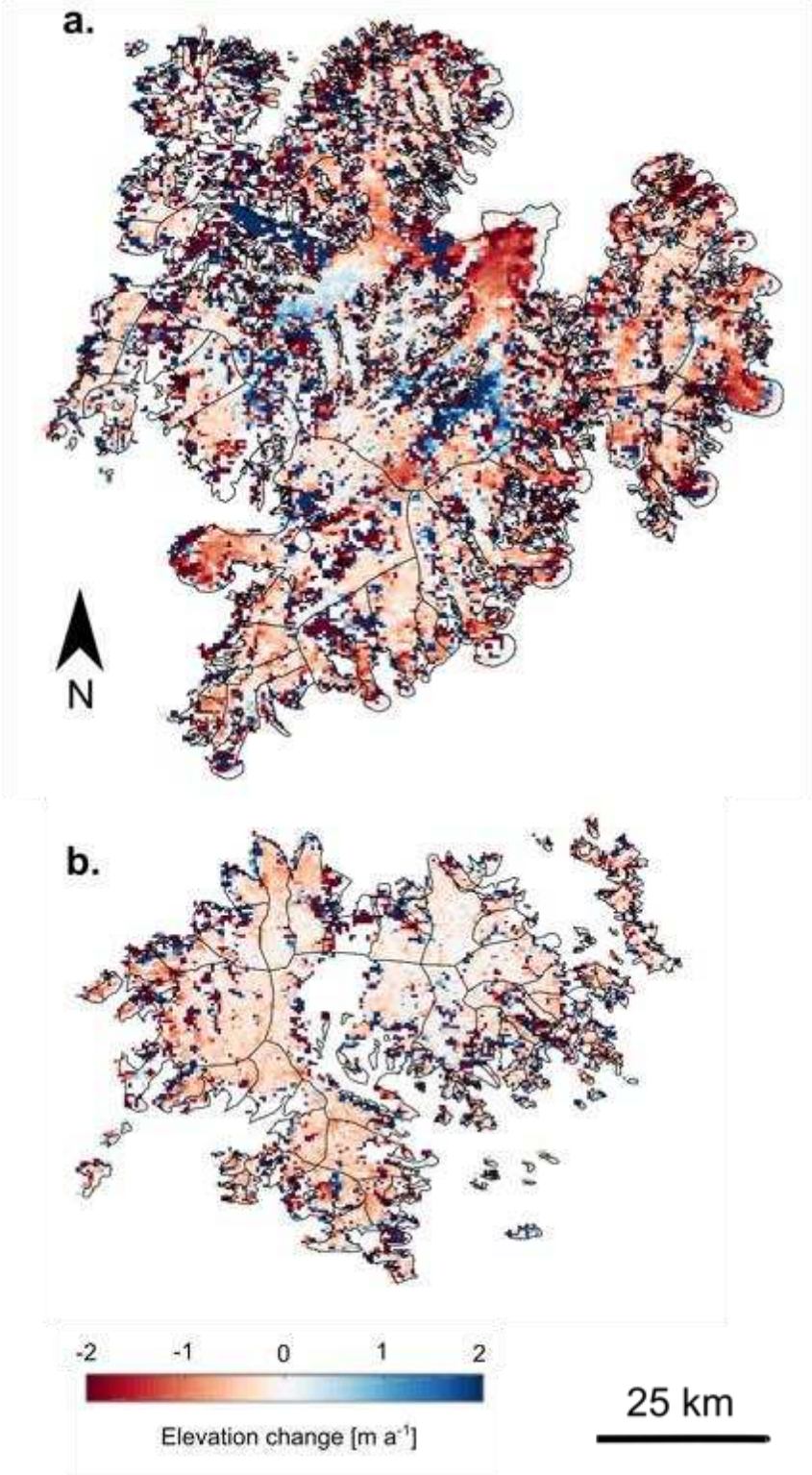
6
7

1 **Appendix C6c.** Surface elevation change rates (2010-2017) over Devon Ice Cap at 500 x 500 m
2 resolution. Spurious elevation changes removed during the post-processing stage are included in
3 the map.
4
5
6
7

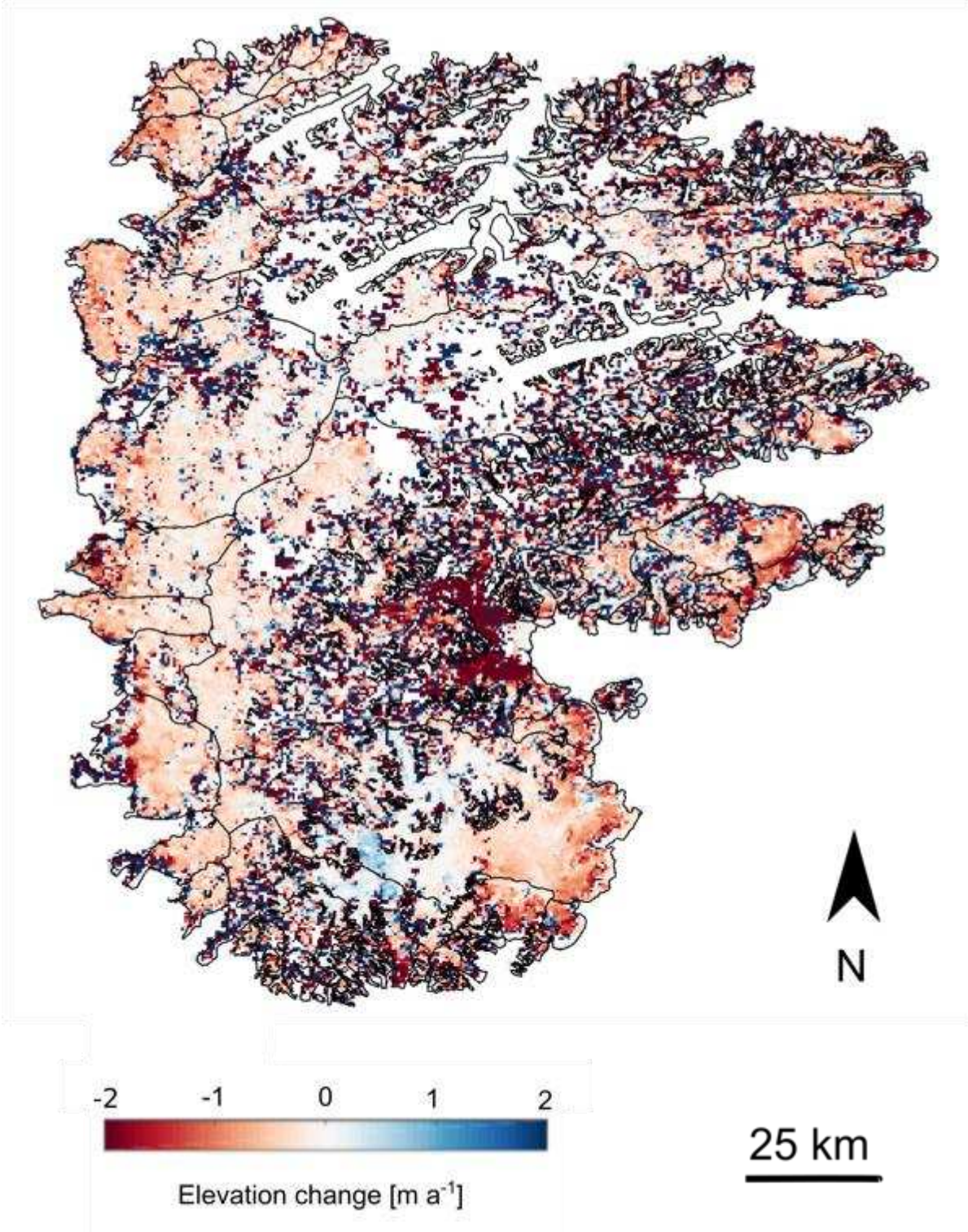


8

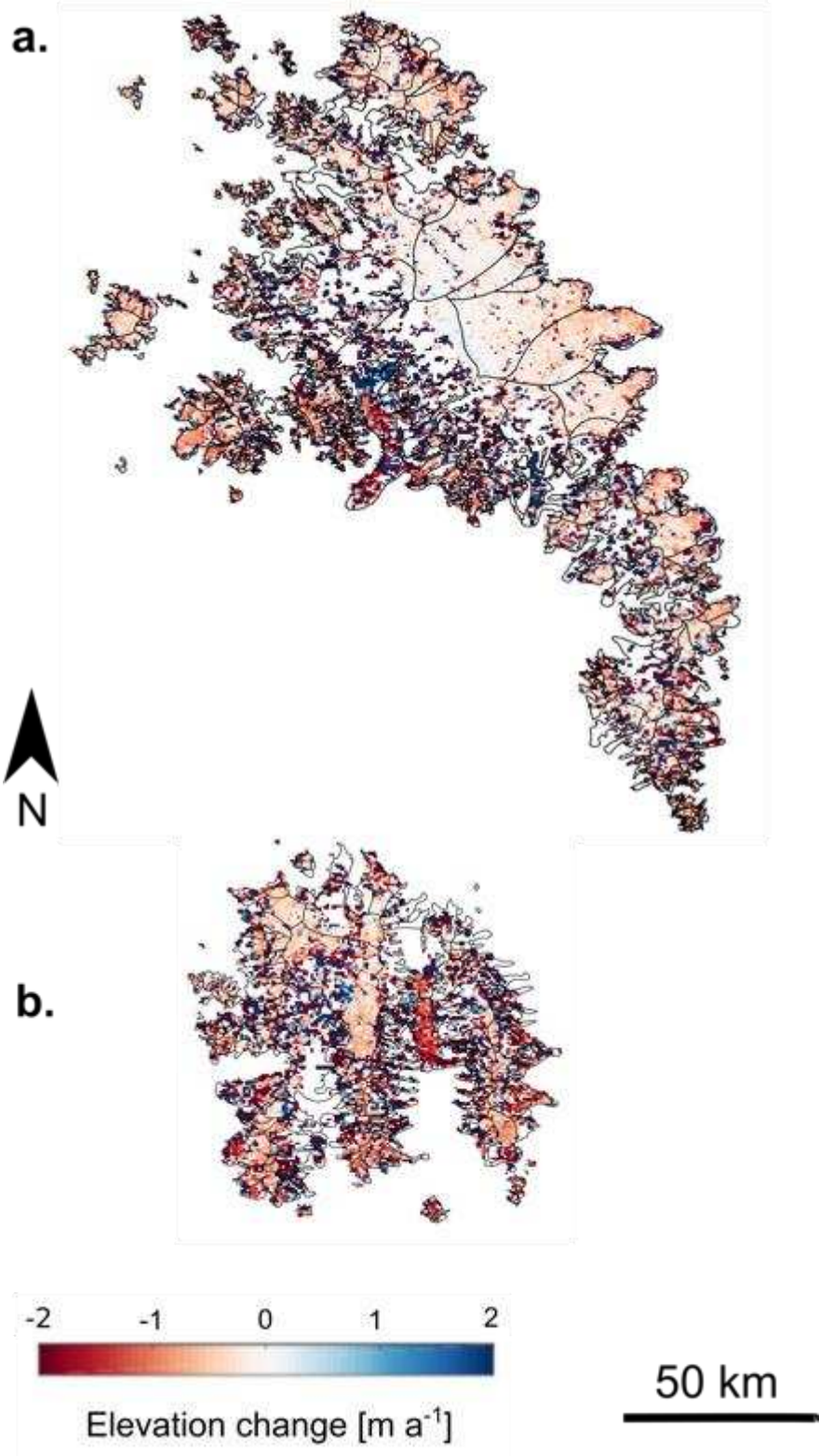
Appendix C6d. Surface elevation change rates (2010-2017) over (a) Manson and (b) Sydkap Ice Caps at 500 x 500 m resolution. Spurious elevation changes removed during the post-processing stage are included in the map.



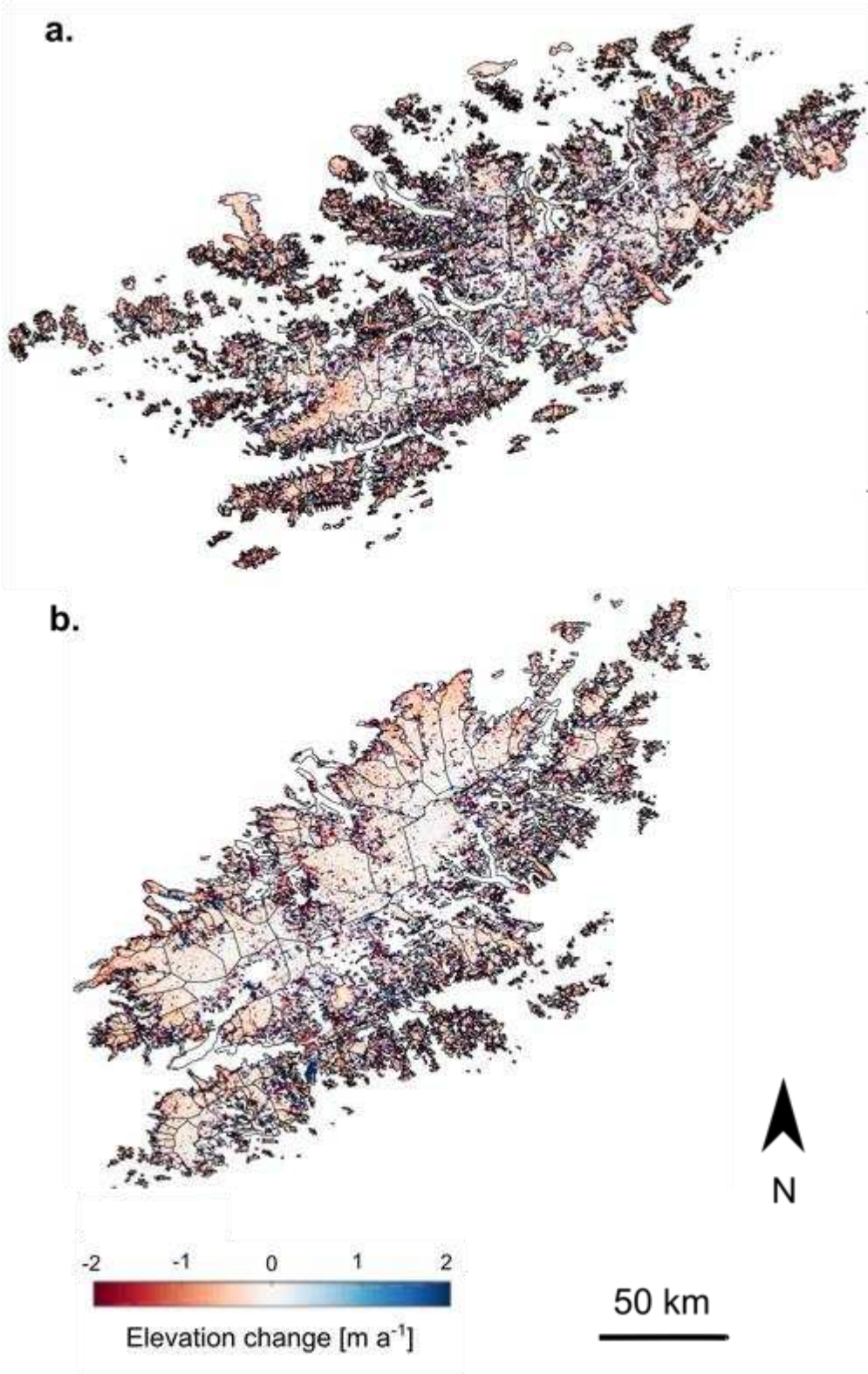
Appendix C6e. Surface elevation change rates (2010-2017) over Prince of Wales Ice Field at 500 x 500 m resolution. Spurious elevation changes removed during the post-processing stage are included in the map.



Appendix C6f. Surface elevation change rates (2010-2017) over (a) Muller and (b) Stacie Ice Caps at 500 x 500 m resolution. Spurious elevation changes removed during the post-processing stage are included in the map.

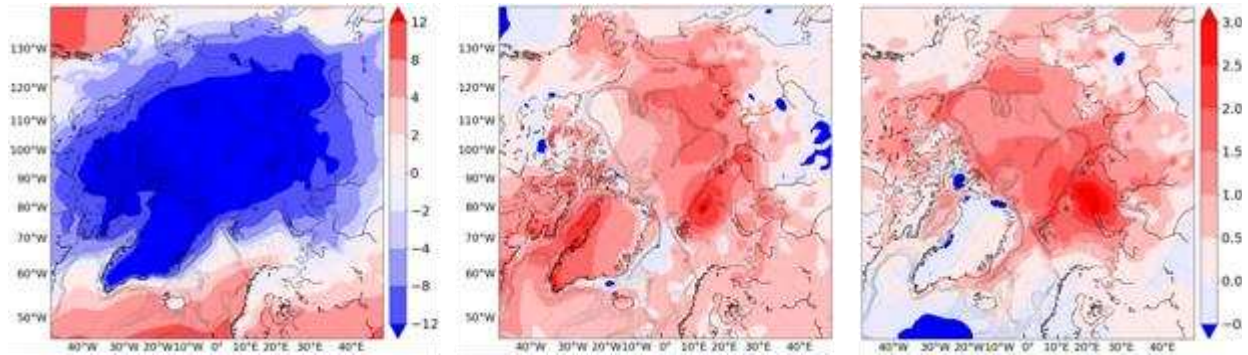


Appendix C6g. Surface elevation change rates (2010-2017) over (a) Northern Ellesmere ice fields and (b) Agassiz Ice Cap at 500 x 500 m resolution. Spurious elevation changes removed during the post-processing stage are included in the map.

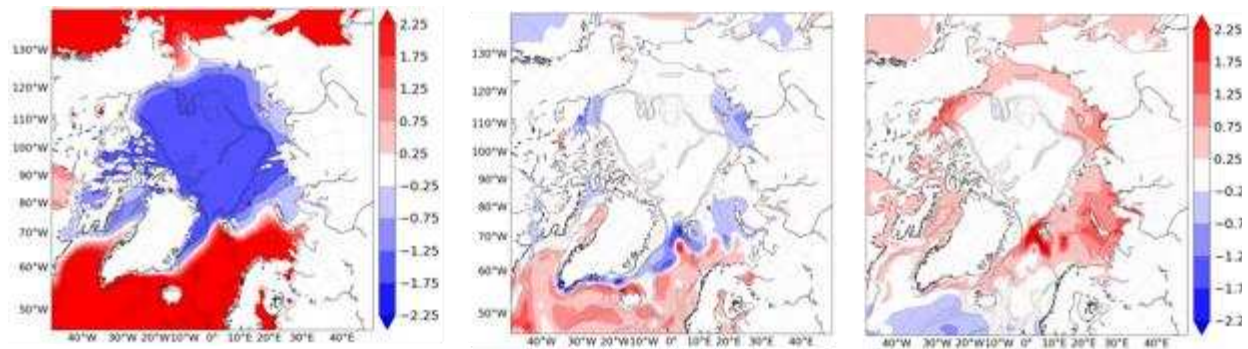


Appendix D. Atmospheric and oceanic forcing anomalies.

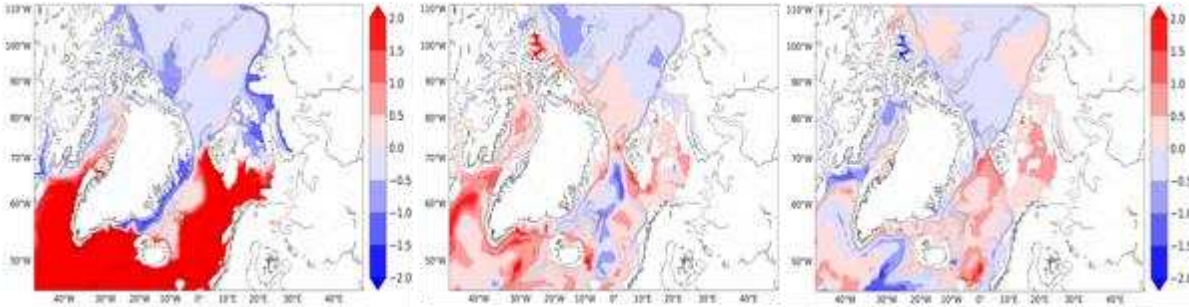
T_{2m} decadal anomalies (ERA-Interim). **Left:** T_{2m} decadal mean of annual means (°C) for the 1990-1999 (baseline) period. **Middle:** T_{2m} anomaly (°C) between the 2000-2009 and the baseline period. **Right:** T_{2m} anomaly (°C) between 2010-2017 and 2000-2009.



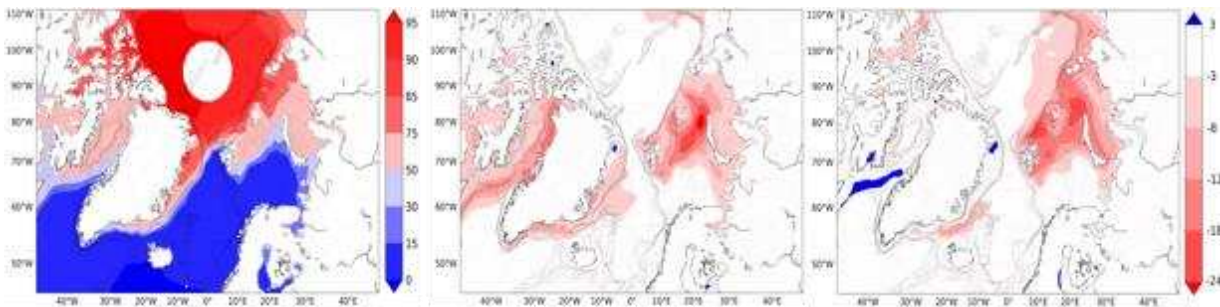
SST decadal anomalies (ERA-Interim). **Left:** SST decadal mean of annual means (°C) for the 1990-1999 (baseline) period. **Middle:** SST anomaly (°C) between the 2000-2009 and the baseline period. **Right:** SST anomaly (°C) between 2010-2017 and 2000-2009.



SOT decadal anomalies (TOPAZ). **Left:** SOT decadal mean of annual means ($^{\circ}\text{C}$) for the 1990-1999 (baseline) period. **Middle:** SOT anomaly ($^{\circ}\text{C}$) between the 2000-2009 and the baseline period. **Right:** SOT anomaly ($^{\circ}\text{C}$) between 2010-2017 and 2000-2009.

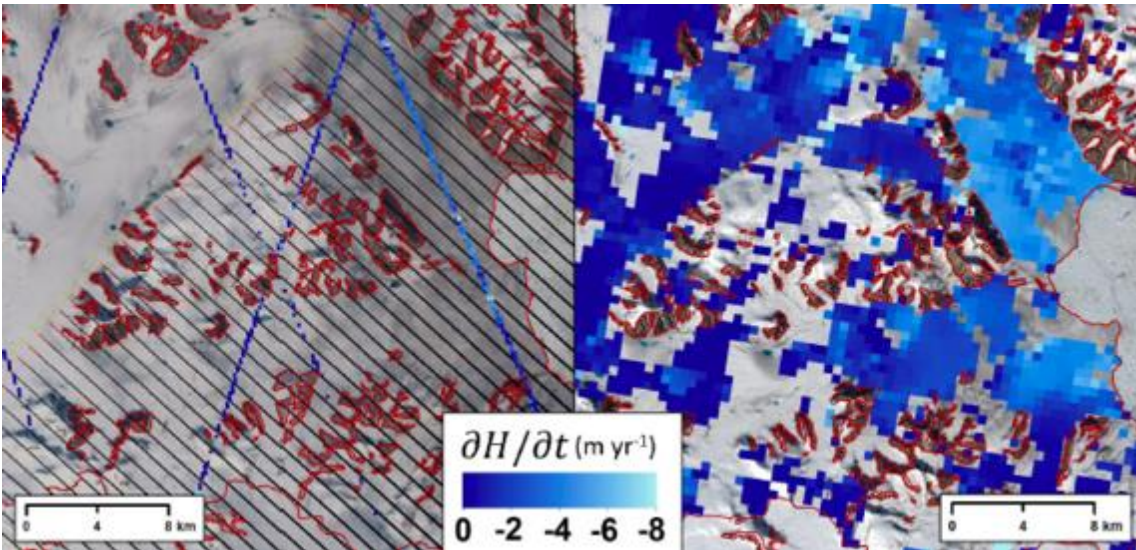


SIC decadal anomalies (NASA Team). **Left:** SIC decadal mean of annual means (%) for the 1990-1999 (baseline) period. **Middle:** SIC anomaly (%) between the 2000-2009 period and the baseline period. **Right:** SIC anomaly (%) between 2010-2017 and 2000-2009.

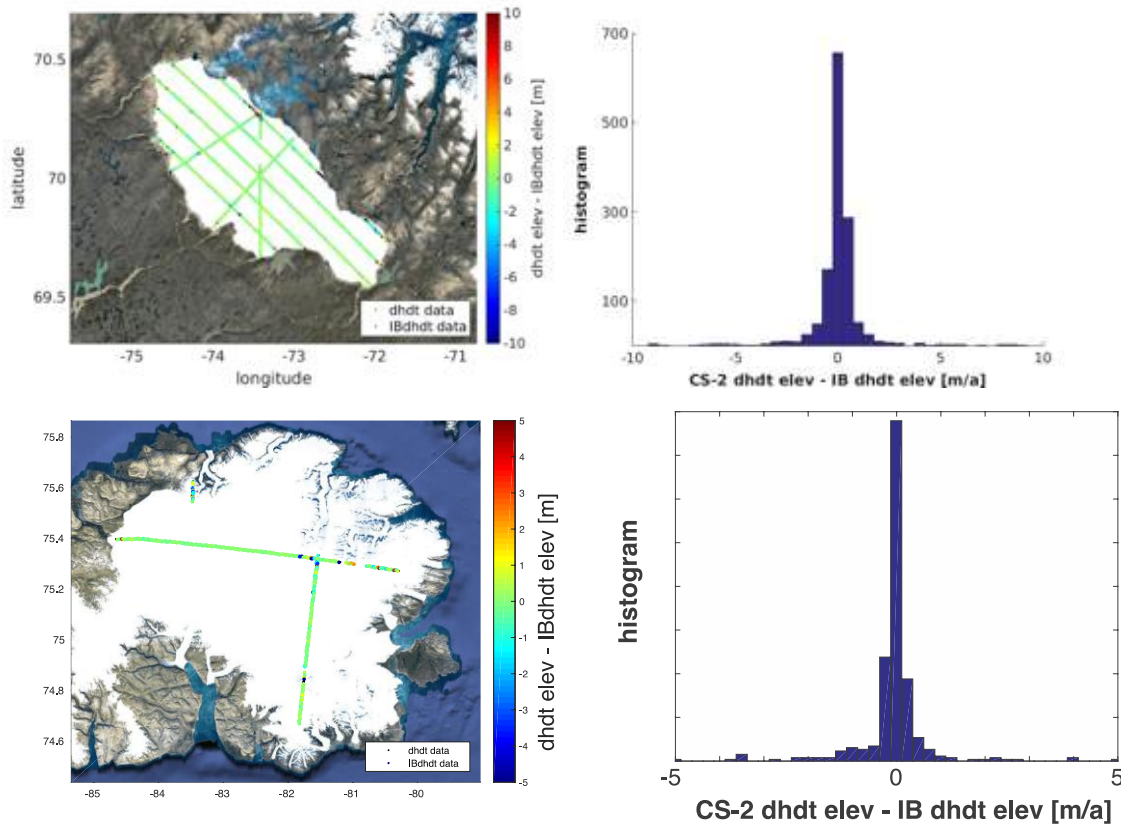


1

Appendix E. Coverage of surface elevation change \dot{h} along ice margins with extreme topography. Example of Trinity-Wykeham Glacier, Nunavut, Canada. ICESat (left panel) for reference, and CryoSat-2 (right panel). Adapted from ref.(Harcourt et al., 2019).



Appendix F. Validation of CryoSat-2 rates of surface elevation change \dot{h} against OIB: Barnes Ice Cap (top panels), and the Devon Ice Cap (bottom panels) with differences of $0.05 \text{ m a}^{-1} \pm 0.26 \text{ m a}^{-1}$ and $0.00 \text{ m a}^{-1} \pm 0.13 \text{ m a}^{-1}$ respectively for Barnes and Devon Ice Caps.



Appendix G. SMB parametrisation coefficients in [10^{-3} a^{-1}]: numbers in brackets for each region indicate the values of lat_ts and lon_0 of the local polar stereographic projection used to calculate the x and y components of the parametrisation of \dot{h} .

Region	a_0	a_1	a_2	a_3	a_4
FJL [80.5 55.0]	$1.7e^{-5}$	$-1.4e^{-2}$	4.5	$1.4e^{-3}$	$2.0e^{-3}$
NZ [75.5 61]	$-2.9e^{-6}$	$4.2e^{-3}$	-0.5	$1.7e^{-3}$	$0.3e^{-3}$
SZ [79.5 99]	$-7.3e^{-7}$	$-1.6e^{-3}$	2.0	$-1.0e^{-3}$	$0.2e^{-3}$
Sv [78.5 20]	$6.3e^{-7}$	$-2.9e^{-3}$	3.8	$1.4 e^{-3}$	$1.6e^{-3}$
Ic [65 -19]	-	-	-	-	-
CAA-N [79 -84]	$-5.3e^{-7}$	$2.0e^{-3}$	-2.0	$0.1 e^{-3}$	$-0.2e^{-3}$
CAA-S [70 -73]	$-4.2e^{-7}$	$1.3e^{-3}$	-0.6	$4.8 e^{-5}$	$0.6e^{-3}$

1

1 References

- 2 Barton, B.I., Lenn, Y.-D., Lique, C., 2018. Observed atlantification of the Barents Sea causes
3 the Polar Front to limit the expansion of winter sea ice. *J. Phys. Oceanogr.* 48, 1849–1866.
4 <https://doi.org/10.1175/jpo-d-18-0003.1>
- 5 Bjørk, A.A., Aagaard, S., Lütt, A., Khan, S.A., Box, J.E., Kjeldsen, K.K., Larsen, N.K.,
6 Korsgaard, N.J., Cappelen, J., Colgan, W.T., Machguth, H., Andresen, C.S., Peings, Y.,
7 Kjær, K.H., 2018. Changes in Greenland’s peripheral glaciers linked to the North Atlantic
8 Oscillation. *Nat. Clim. Chang.* 8, 48–52. <https://doi.org/10.1038/s41558-017-0029-1>
- 9 Blaszczyk, M., Jania, J.A., Hagen, J.O., 2009. Tidewater glaciers of Svalbard: Recent changes
10 and estimates of calving fluxes, *Polish Polar Research*.
- 11 Byrne, M.P., Schneider, T., 2018. Atmospheric dynamics feedback: concept, simulations and
12 climate implications. *J. Clim.* 31, 3249–3264. <https://doi.org/10.1175/JCLI-D-17-0470.1>
- 13 Carr, J.R., Bell, H., Killick, R., Holt, T., 2017. Exceptional retreat of Novaya Zemlya’s marine-
14 terminating outlet glaciers between 2000 and 2013. *Cryosph.* 11, 2149–2174.
15 <https://doi.org/10.5194/tc-11-2149-2017>
- 16 Cavalieri, D., Parkinson, C., Gloersen, P., Zwally, J.H., 2019. Sea ice concentrations from
17 Nimbus-7 SMMR and DMSP SSM/I-SSMIS passive microwave data, Version 1. Boulder,
18 Colorado USA.
- 19 Christie, F.D.W., Bingham, R.G., Gourmelen, N., Tett, S.F.B., Muto, A., 2016. Four-decade
20 record of pervasive grounding line retreat along the Bellingshausen margin of West
21 Antarctica. *Geophys. Res. Lett.* 43, 5741–5749. <https://doi.org/10.1002/2016GL068972>
- 22 Church, J.A. et al., 2013. *Climate Change 2013: The Physical Science Basis. Contribution of*
23 *Working Group I to the Fifth Assessment Report of the Intergovernmental Panel on Climate*
24 *Change (IPCC).* Cambridge Univ. Press, Cambridge.
- 25 Ciraci, E., Velicogna, I., Sutterley, T.C., 2018. Mass Balance of Novaya Zemlya Archipelago,
26 Russian high arctic, using time-variable gravity from GRACE and altimetry data from
27 ICESat and CryoSat-2. *Remote Sens.* 10. <https://doi.org/10.3390/rs10111817>
- 28 Ciraci, E., Velicogna, I., Swenson, S., 2020. Continuity of the Mass Loss of the World ’ s
29 Glaciers and Ice Caps From the GRACE and GRACE Follow-On Missions. *Geophys. Res.*
30 *Lett.* 47, 1–11. <https://doi.org/10.1029/2019GL086926>
- 31 Comiso, J.C., 2017. Bootstrap sea ice concentrations from Nimbus-7 SMMR and DMSP SSM/I-
32 SSMIS, Version 3. Boulder, Colorado USA.
- 33 Cook, A.J., Copland, L., Noël, B.P.Y., Stokes, C.R., Bentley, M.J., Sharp, M.J., Bingham, R.G.,
34 van den Broeke, M.R., 2019. Atmospheric forcing of rapid marine-terminating glacier
35 retreat in the Canadian Arctic Archipelago. *Sci. Adv.* 5, 8507.
36 <https://doi.org/10.1126/sciadv.aau8507>
- 37 Cowton, T.R., Sole, A.J., Nienow, P.W., Slater, D.A., Christoffersen, P., 2018. Linear response
38 of east Greenland’s tidewater glaciers to ocean/atmosphere warming. *Proc. Natl. Acad.*
39 *Sci.* 115, 7907–7912. <https://doi.org/10.1073/pnas.1801769115>
- 40 Cuffey, K.M., Paterson, W.S.B., 2010. *The Physics of Glaciers*, 4th ed. ed. Elsevier,
41 Amsterdam.
- 42 Dee, D.P., Uppala, S.M., Simmons, A.J., Berrisford, P., Poli, P., Kobayashi, S., Andrae, U.,
43 Balmaseda, M.A., Balsamo, G., Bauer, P., Bechtold, P., Beljaars, A.C.M., van de Berg, L.,
44 Bidlot, J., Bormann, N., Delsol, C., Dragani, R., Fuentes, M., Geer, A.J., Haimberger, L.,
45 Healy, S.B., Hersbach, H., Hólm, E. V., Isaksen, L., Kållberg, P., Köhler, M., Matricardi, M.,
46 Mcnally, A.P., Monge-Sanz, B.M., Morcrette, J.J., Park, B.K., Peubey, C., de Rosnay, P.,
47 Tavolato, C., Thépaut, J.N., Vitart, F., 2011. The ERA-Interim reanalysis: Configuration and
48 performance of the data assimilation system. *Q. J. R. Meteorol. Soc.* 137, 553–597.
49 <https://doi.org/10.1002/qj.828>
- 50 Delhasse, A., Fettweis, X., Kittel, C., Amory, C., Agosta, C., 2018. Brief communication: Impact

- 1 of the recent atmospheric circulation change in summer on the future surface mass
2 balance of the Greenland Ice Sheet. *Cryosphere* 12, 3409–3418. [https://doi.org/10.5194/tc-](https://doi.org/10.5194/tc-12-3409-2018)
3 [12-3409-2018](https://doi.org/10.5194/tc-12-3409-2018)
- 4 Ding, Q., Wallace, J.M., Battisti, D.S., Steig, E.J., Gallant, A.J.E., Kim, H.-J., Geng, L., 2014.
5 Tropical forcing of the recent rapid Arctic warming in northeastern Canada and Greenland.
6 *Nature* 509, 209–212. <https://doi.org/10.1038/nature13260>
- 7 Dunse, T., Schellenberger, T., Hagen, J.O., Käab, A., Schuler, T. V., Reijmer, C.H., 2015.
8 Glacier-surge mechanisms promoted by a hydro-thermodynamic feedback to summer melt.
9 *Cryosphere* 9, 197–215. <https://doi.org/10.5194/tc-9-197-2015>
- 10 Enderlin, E.M., Howat, I.M., Jeong, S., Noh, M.-J., van Angelen, J.H., van den Broeke, M.R.,
11 2014. An improved mass budget for the Greenland ice sheet. *Geophys. Res. Lett.* 41, 866–
12 872.
- 13 Farinotti, D., Huss, M., Fürst, J.J., Landmann, J., Machguth, H., Maussion, F., Pandit, A., 2019.
14 A consensus estimate for the ice thickness distribution of all glaciers on Earth. *Nat. Geosci.*
15 12, 168–173. <https://doi.org/10.1038/s41561-019-0300-3>
- 16 Foresta, L., Gourmelen, N., Pálsson, F., Nienow, P., Björnsson, H., Shepherd, A., 2016. Surface
17 elevation change and mass balance of Icelandic ice caps derived from swath mode
18 CryoSat-2 altimetry. *Geophys. Res. Lett.* 43, 12138–12145.
19 <https://doi.org/10.1002/2016GL071485>
- 20 Foresta, L., Gourmelen, N., Weissgerber, F., Nienow, P., Williams, J.J., Shepherd, A.,
21 Drinkwater, M.R., Plummer, S., 2018. Heterogeneous and rapid ice loss over the
22 Patagonian Ice Fields revealed by CryoSat-2 swath radar altimetry. *Remote Sens. Environ.*
23 211, 441–455. <https://doi.org/10.1016/j.rse.2018.03.041>
- 24 Gardner, A.S., Moholdt, G., Arendt, A., Wouters, B., 2012. Accelerated contributions of
25 Canada's Baffin and Bylot Island glaciers to sea level rise over the past half century.
26 *Cryosph.* 6, 1103–1125. <https://doi.org/10.5194/tc-6-1103-2012>
- 27 Gardner, A.S., Moholdt, G., Cogley, J.G., Wouters, B., Arendt, A. a., Wahr, J., Berthier, E.,
28 Hock, R., Pfeffer, W.T., Kaser, G., Ligtenberg, S.R.M., Bolch, T., Sharp, M.J., Hagen, J.O.,
29 van den Broeke, M.R., Paul, F., 2013. A reconciled estimate of glacier contributions to sea
30 level rise: 2003 to 2009. *Science* (80-.). 340, 852–857.
31 <https://doi.org/10.1126/science.1234532>
- 32 Gardner, A.S., Moholdt, G., Wouters, B., Wolken, G.J., Burgess, D.O., Sharp, M.J., Cogley,
33 J.G., Braun, C., Labine, C., 2011. Sharply increased mass loss from glaciers and ice caps
34 in the Canadian Arctic Archipelago. *Nature* 473, 357–360.
35 <https://doi.org/10.1038/nature10089>
- 36 Gardner, A.S., Sharp, M., 2006. Influence of the Arctic Circumpolar Vortex on the mass balance
37 of Canadian High Arctic glaciers. *J. Clim.* 20, 4586–4598.
38 <https://doi.org/10.1175/JCLI4268.1>
- 39 Glazovskiy, A.F., 1996. Mass Balance of Arctic Glaciers, IASC Report No. 5. University of
40 Silesia, Sosnowiec-Oslo, Norway.
- 41 Gourmelen, N., Escorihuela, M.J., Shepherd, A., Foresta, L., Muir, A., Garcia-Mondéjar, A.,
42 Roca, M., Baker, S.G., Drinkwater, M.R., 2018. CryoSat-2 swath interferometric altimetry
43 for mapping ice elevation and elevation change. *Adv. Sp. Res.* 62, 1226–1242.
44 <https://doi.org/10.1016/j.asr.2017.11.014>
- 45 Gray, L., Burgess, D., Copland, L., Cullen, R., Galin, N., Hawley, R., Helm, V., 2013.
46 Interferometric swath processing of Cryosat data for glacial ice topography. *Cryosphere* 7,
47 1857–1867. <https://doi.org/10.5194/tc-7-1857-2013>
- 48 Gray, L., Burgess, D., Copland, L., Demuth, M.N., Dunse, T., Langley, K., Schuler, T. V., 2015.
49 CryoSat-2 delivers monthly and inter-annual surface elevation change for Arctic ice caps.
50 *Cryosph.* 9, 1895–1913. <https://doi.org/10.5194/tcd-9-2821-2015>
- 51 Haga, O.N., McNabb, R., Nuth, C., Altena, B., Schellenberger, T., Käab, A., 2020. From high

1 friction zone to frontal collapse: Dynamics of an ongoing tidewater glacier surge,
2 Negribreen, Svalbard. *J. Glaciol.* 66, 742–754. <https://doi.org/10.1017/jog.2020.43>

3 Harcourt, W.D., Palmer, S.J., Mansell, D.T., Brocq, A. Le, Bartlett, O., Gourmelen, N., Tepes,
4 P., Dowdeswell, J.A., Donald, D., Young, D.A., Harcourt, W.D., Palmer, S.J., Mansell, D.T.,
5 Brocq, A. Le, Bartlett, O., Gourmelen, N., Tepes, P., Dowdeswell, J.A., Blankenship, D.D.,
6 2019. Subglacial controls on dynamic thinning at Trinity- Wykeham Glacier , Prince of
7 Wales Ice Field , Canadian Arctic. *Int. J. Remote Sens.* 00, 1–23.
8 <https://doi.org/10.1080/01431161.2019.1658238>

9 Huss, M., 2013. Density assumptions for converting geodetic glacier volume change to mass
10 change. *Cryosph.* 7, 877–887. <https://doi.org/10.5194/tcd-7-219-2013>

11 Ignécz, Á., Sole, A.J., Livingstone, S.J., Leeson, A.A., Fettweis, X., Selmes, N., Gourmelen, N.,
12 Briggs, K., 2016. Northeast sector of the Greenland Ice Sheet to undergo the greatest
13 inland expansion of supraglacial lakes during the 21st century. *Geophys. Res. Lett.* 43,
14 9729–9738. <https://doi.org/10.1002/2016GL070338>

15 Labe, Z., Magnúsdóttir, G., Stern, H., 2018. Variability of Arctic sea ice thickness using PIOMAS
16 and the CESM Large Ensemble. *J. Clim.* 31, 3233–3247. <https://doi.org/10.1175/JCLI-D-17-0436.1>

17
18 Lind, S., Ingvaldsen, R.B., Furevik, T., 2018. Arctic warming hotspot in the northern Barents Sea
19 linked to declining sea-ice import. *Nat. Clim. Chang.* 8, 634–639.
20 <https://doi.org/10.1038/s41558-018-0205-y>

21 Lindsay, R., Wensnahan, M., Schweiger, A., Zhang, J., 2014. Evaluation of seven different
22 atmospheric reanalysis products in the Arctic*. *J. Clim.* 27, 2588–2606.
23 <https://doi.org/10.1175/JCLI-D-13-00014.1>

24 Martin, T., Adcroft, A., 2010. Parameterizing the fresh-water flux from land ice to ocean with
25 interactive icebergs in a coupled climate model. *Ocean Model.* 34, 111–124.
26 <https://doi.org/10.1016/j.ocemod.2010.05.001>

27 McMillan, M., Shepherd, A., Gourmelen, N., Dehecq, A., Leeson, A., Ridout, A., Flament, T.,
28 Hogg, A., Gilbert, L., Benham, T., van den Broeke, M., Dowdeswell, J.A., Fettweis, X.,
29 Noel, B., Strozzi, T., 2014. Rapid dynamic activation of a marine-based Arctic ice cap.
30 *Geophys. Res. Lett.* 41, 8902–8909. <https://doi.org/10.1002/2014GL062255>

31 Melkonian, A.K., Willis, M.J., Pritchard, M.E., Stewart, A.J., 2016. Recent changes in glacier
32 velocities and thinning at Novaya Zemlya. *Remote Sens. Environ.* 174, 244–257.
33 <https://doi.org/10.1016/j.rse.2015.11.001>

34 Millan, R., Mougnot, J., Rignot, E., 2017. Mass budget of the glaciers and ice caps of the
35 Queen Elizabeth Islands, Canada, from 1991 to 2015. *Environ. Res. Lett.* 12, 024016.

36 Moholdt, G., 2010. Elevation change and mass balance of Svalbard glaciers from geodetic data.
37 PhD Thesis 94.

38 Moholdt, G., Heid, T., Benham, T., Dowdeswell, J.A., 2012a. Dynamic instability of marine-
39 terminating glacier basins of Academy of Sciences Ice Cap, Russian High Arctic. *Ann.*
40 *Glaciol.* 53, 193–201. <https://doi.org/10.3189/2012AoG60A117>

41 Moholdt, G., Wouters, B., Gardner, A.S., 2012b. Recent mass changes of glaciers in the
42 Russian High Arctic. *Geophys. Res. Lett.* 39, L10502.
43 <https://doi.org/10.1029/2012GL051466>

44 Möller, M., Navarro, F., Martín-Español, A., 2016. Monte Carlo modelling projects the loss of
45 most land-terminating glaciers on Svalbard in the 21st century under RCP 8.5 forcing.
46 *Environ. Res. Lett.* 11, 094006. <https://doi.org/10.1088/1748-9326/11/9/094006>

47 Morris, A., Moholdt, G., Gray, L., 2020. Spread of Svalbard Glacier Mass Loss to Barents Sea
48 Margins Revealed by CryoSat-2. *J. Geophys. Res. Earth Surf.* 125.
49 <https://doi.org/10.1029/2019JF005357>

50 Mortimer, C.A., Sharp, M., Van Wychen, W., 2018. Influence of recent warming and ice
51 dynamics on glacier surface elevations in the Canadian High Arctic, 1995–2014. *J. Glaciol.*

64, 450–464. <https://doi.org/10.1017/jog.2018.37>

1 Mouginit, J., Rignot, E., Bjørk, A.A., van den Broeke, M., Millan, R., Morlighem, M., Noël, B.,
2 Scheuchl, B., Wood, M., 2019. Forty-six years of Greenland Ice Sheet mass balance from
3 1972 to 2018. *Proc. Natl. Acad. Sci.* 116, 9239–9244.
4 <https://doi.org/10.1073/pnas.1904242116>

5 Nick, F.M., Vieli, A., Andersen, M.L., Joughin, I., Payne, A., Edwards, T.L., Pattyn, F., Van De
6 Wal, R.S.W., 2013. Future sea-level rise from Greenland’s main outlet glaciers in a
7 warming climate. *Nature* 497, 235–238. <https://doi.org/10.1038/nature12068>

8 Nilsson, J., Gardner, A., Sørensen, L.S., Forsberg, R., 2016. Improved retrieval of land ice
9 topography from CryoSat-2 data and its impact for volume-change estimation of the
10 Greenland Ice Sheet. *Cryosphere* 10, 2953–2969. <https://doi.org/10.5194/tc-10-2953-2016>

11 Noël, B., van de Berg, W.J., Lhermitte, S., Wouters, B., Schaffer, N., van den Broeke, M.R.,
12 2018. Six decades of glacial mass loss in the Canadian Arctic Archipelago. *J. Geophys.*
13 *Res. Earth Surf.* 123, 1430–1449. <https://doi.org/10.1029/2017JF004304>

14 Nuth, C., Gilbert, A., Köhler, A., McNabb, R., Schellenberger, T., Sevestre, H., Weidle, C.,
15 Girod, L., Luckman, A., Kääb, A., 2019. Dynamic vulnerability revealed in the collapse of
16 an Arctic tidewater glacier. *Sci. Rep.* 9, 5541. <https://doi.org/10.1038/s41598-019-41117-0>

17 Onarheim, I.H., Eldevik, T., Smedsrud, L.H., Stroeve, J.C., 2018. Seasonal and regional
18 manifestation of Arctic sea ice loss. *J. Clim.* 31, 4917–4932. [https://doi.org/10.1175/JCLI-](https://doi.org/10.1175/JCLI-D-17-0427.1)
19 [D-17-0427.1](https://doi.org/10.1175/JCLI-D-17-0427.1)

20 Polyakov, I. V., Pnyushkov, A. V., Alkire, M.B., Ashik, I.M., Baumann, T.M., Carmack, E.C.,
21 Goszczko, I., Guthrie, J., Ivanov, V. V., Kanzow, T., Krishfield, R., Kwok, R., Sundfjord, A.,
22 Morison, J., Rember, R., Yulin, A., 2017. Greater role for Atlantic inflows on sea-ice loss in
23 the Eurasian Basin of the Arctic Ocean. *Science* (80-.). 356, 285–291.
24 <https://doi.org/10.1126/science.aai8204>

25 Price, S.F., Payne, A.J., Howat, I.M., Smith, B.E., 2011. Committed sea-level rise for the next
26 century from Greenland ice sheet dynamics during the past decade. *Proc. Natl. Acad. Sci.*
27 108, 8978–8983. <https://doi.org/10.1073/pnas.1017313108>

28 Radić, V., Bliss, A., Beedlow, A.C., Hock, R., Miles, E., Cogley, J.G., 2014. Regional and global
29 projections of twenty-first century glacier mass changes in response to climate scenarios
30 from global climate models. *Clim. Dyn.* 42, 37–58. [https://doi.org/10.1007/s00382-013-](https://doi.org/10.1007/s00382-013-1719-7)
31 [1719-7](https://doi.org/10.1007/s00382-013-1719-7)

32 Robel, A.A., 2017. Thinning sea ice weakens buttressing force of iceberg mélange and
33 promotes calving. *Nat. Commun.* 8, 14596. <https://doi.org/10.1038/ncomms14596>

34 Rolstad, C., Haug, T., Denby, B., 2009. Spatially integrated geodetic glacier mass balance and
35 its uncertainty based on geostatistical analysis: Application to the western Svartisen ice
36 cap, Norway. *J. Glaciol.* 55, 666–680. <https://doi.org/10.3189/002214309789470950>

37 Sánchez-Gómez, P., Navarro, F.J., Benham, T.J., Glazovsky, A.F., Bassford, R.P.,
38 Dowdeswell, J.A., 2019. Intra- and inter-annual variability in dynamic discharge from the
39 Academy of Sciences Ice Cap, Severnaya Zemlya, Russian Arctic, and its role in
40 modulating mass balance. *J. Glaciol.* 65, 780–797. <https://doi.org/10.1017/jog.2019.58>

41 Schuler, T. V., Kohler, J., Elagina, N., Hagen, J.O.M., Hodson, A.J., Jania, J.A., Kääb, A.M.,
42 Luks, B., Małeckki, J., Moholdt, G., Pohjola, V.A., Sobota, I., Van Pelt, W.J.J., 2020.
43 Reconciling Svalbard Glacier Mass Balance. *Front. Earth Sci.* 8, 1–16.
44 <https://doi.org/10.3389/feart.2020.00156>

45 Shindell, D., Faluvegi, G., 2009. Climate response to regional radiative forcing during the
46 twentieth century. *Nat. Geosci.* 2, 294–300. <https://doi.org/10.1038/ngeo473>

47 Slater, D.A., Goldberg, D.N., Nienow, P.W., Cowton, T.R., 2016. Scalings for submarine melting
48 at tidewater glaciers from buoyant plume theory. *J. Phys. Oceanogr.* 46, 1839–1855.
49 <https://doi.org/10.1175/jpo-d-15-0132.1>

50 Strozzi, T., Kääb, A., Schellenberger, T., 2017a. Frontal destabilization of Stonebreen,
51

1 Edgeøya, Svalbard. *Cryosphere* 11, 553–566. <https://doi.org/10.5194/tc-11-553-2017>

2 Strozzi, T., Paul, F., Wiesmann, A., Schellenberger, T., Kääb, A., 2017b. Circum-arctic changes
3 in the flow of glaciers and ice caps from satellite SAR data between the 1990s and 2017.
4 *Remote Sens.* 9. <https://doi.org/10.3390/rs9090947>

5 Studinger, M., 2014. IceBridge ATM L4 Surface Elevation Rate of Change, Version 1. Boulder,
6 Colorado USA. <https://doi.org/https://doi.org/10.5067/BCW6CI3TXOCY>

7 Thornalley, D.J.R., Delia, W., Ortega, P., Robson, J.I., Brierley, C.M., Davis, R., Hall, I.R.,
8 Moffa-sanchez, P., Rose, N.L., Spooner, P.T., Yashayaev, I., Keigwin, L.D., 2018. Atlantic
9 overturning during the past 150 years. *Nature* 556, 227–230.
10 <https://doi.org/10.1038/s41586-018-0007-4>

11 Willis, M.J., Melkonian, A.K., Pritchard, M.E., 2015. Outlet glacier response to the 2012 collapse
12 of the Matusevich Ice Shelf, Severnaya Zemlya, Russian Arctic. *J. Geophys. Res. Earth*
13 *Surf.* 120, 2040–2055. <https://doi.org/10.1002/2015JF003544>

14 Willis, M.J., Zheng, W., Durkin, W.J., Pritchard, M.E., Ramage, J.M., Dowdeswell, J.A.,
15 Benham, T.J., Bassford, R.P., Stearns, L.A., Glazovsky, A.F., Macheret, Y.Y., Porter, C.C.,
16 2018. Massive destabilization of an Arctic ice cap. *Earth Planet. Sci. Lett.* 502, 146–155.
17 <https://doi.org/10.1016/j.epsl.2018.08.049>

18 Wingham, D.J., Francis, C.R., Baker, S., Bouzinac, C., Brockley, D., Cullen, R., de Chateau-
19 Thierry, P., Laxon, S.W., Mallow, U., Mavrocordatos, C., Phalippou, L., Ratier, G., Rey, L.,
20 Rostan, F., Viau, P., Wallis, D.W., 2006. CryoSat: A mission to determine the fluctuations
21 in Earth's land and marine ice fields. *Adv. Sp. Res.* 37, 841–871.
22 <https://doi.org/10.1016/j.asr.2005.07.027>

23 Wouters, B., Gardner, A.S., Moholdt, G., 2019. Global glacier mass loss during the GRACE
24 satellite mission (2002-2016). *Front. Earth Sci.* 7, 1–11.
25 <https://doi.org/10.3389/feart.2019.00096>

26 Xie, J., Bertino, L., Knut, L., Sakov, P., 2017. Quality assessment of the TOPAZ4 reanalysis in
27 the Arctic over the period 1991-2013. *Ocean Sci.* 13, 123–144. [https://doi.org/10.5194/os-](https://doi.org/10.5194/os-13-123-2017)
28 [13-123-2017](https://doi.org/10.5194/os-13-123-2017)

29 Yang, Q., Dixon, T.H., Myers, P.G., Bonin, J., Chambers, D., Van Den Broeke, M.R., 2016.
30 Recent increases in Arctic freshwater flux affects Labrador Sea convection and Atlantic
31 overturning circulation. *Nat. Commun.* 7. <https://doi.org/10.1038/ncomms10525>

32 Zeeberg, J., Forman, S.L., 2001. Changes in glacier extent on north Novaya Zemlya in the
33 twentieth century. *The Holocene* 11, 161–175.
34 <https://doi.org/10.1191/095968301676173261>

35 Zemp, M., Huss, M., Thibert, E., Eckert, N., McNabb, R., Huber, J., Barandun, M., Machguth,
36 H., Nussbaumer, S.U., Gärtner-Roer, I., Thomson, L., Paul, F., Maussion, F., Kutuzov, S.,
37 Cogley, J.G., 2019. Global glacier mass changes and their contributions to sea-level rise
38 from 1961 to 2016. *Nature* 568, 382–386. <https://doi.org/10.1038/s41586-019-1071-0>

39 Zheng, W., Pritchard, M.E., Willis, M.J., Stearns, L.A., 2019. The Possible Transition From
40 Glacial Surge to Ice Stream on Vavilov Ice Cap. *Geophys. Res. Lett.* 46, 13892–13902.
41 <https://doi.org/10.1029/2019GL084948>

42 Zheng, W., Pritchard, M.E., Willis, M.J., Tepes, P., Gourmelen, N., Benham, T.J., Dowdeswell,
43 J.A., 2018. Accelerating glacier mass loss on Franz Josef Land, Russian Arctic. *Remote*
44 *Sens. Environ.* 211, 357–375.

45